JCB Journal of Cell Biology

TOOLS

Fluorescence lifetime sorting reveals tunable enzyme interactions within cytoplasmic condensates

Leyla E. Fahim[1***], Joshua M. Marcus[1***], Noah D. Powell[1], Zachary A. Ralston[1], Katherine Walgamotte[1], Eleonora Perego[3], Giuseppe Vicidomini[3], Alessandro Rossetta[4], and Jason E. Lee[1,2]

Ribonucleoprotein (RNP) condensates partition RNA and protein into multiple liquid phases. The multiphasic feature of condensate-enriched components creates experimental challenges for distinguishing membraneless condensate functions from the surrounding dilute phase. We combined fluorescence lifetime imaging microscopy (FLIM) with phasor plot filtering and segmentation to resolve condensates from the dilute phase. Condensate-specific lifetimes were used to track protein–protein interactions by measuring FLIM–Förster resonance energy transfer (FRET). We used condensate FLIM-FRET to evaluate whether mRNA decapping complex subunits can form decapping-competent interactions within P-bodies. Condensate FLIM-FRET revealed the presence of core subunit interactions within P-bodies under basal conditions and the disruption of interactions between the decapping enzyme (Dcp2) and a critical cofactor (Dcp1A) during oxidative stress. Our results show a context-dependent plasticity of the P-body interaction network, which can be rewired within minutes in response to stimuli. Together, our FLIM-based approaches provide investigators with an automated and rigorous method to uncover and track essential protein–protein interaction dynamics within RNP condensates in live cells.

Introduction

The RNA life cycle is associated with an array of membraneless organelles known as ribonucleoprotein (RNP) condensates (Banani et al., 2016; Alberti and Hyman, 2021). Evolutionarily conserved RNP condensates impact RNA metabolism by compartmentalizing the aqueous spaces of membrane-bound organelles. Nucleoli, Cajal bodies, and nuclear speckles catalyze ribosome assembly, transcription, and splicing in the nucleus, respectively (Banani et al., 2016; Alberti and Hyman, 2021). Mitochondrial granules maintain RNA stability in the mitochondria (Jourdain et al., 2013; Antonicka et al., 2013). In the cytoplasm, mRNA processing (P)-bodies are enriched with factors associated with mRNA sequestration, silencing, editing, and decay (Decker and Parker, 2012; Hubstenberger et al., 2017). Despite the reconstitution and functional characterization of many RNA processing enzyme complexes in vitro (Jonas and Izaurralde, 2013; Chang et al., 2014; Tibble et al., 2021; Schirle et al., 2014; Cho et al., 2003), the co-existence of condensate-enriched enzyme complexes within the surrounding milieu at dilute, non-negligible concentrations has obscured the full impact of many RNP condensates on cellular function. Furthermore, there are technical hurdles associated with isolating or reconstituting RNP condensates for functional assays (Hubstenberger et al., 2017; Freibaum et al., 2021; Currie et al., 2023). Therefore, distinguishing RNP condensate functions from dilute phase functions requires the development of new tools and approaches to bridge existing biochemical studies on enzyme function with condensate-level resolution in live cells.

Conventional fluorescence microscopy approaches measure fluorescence as a function of photon counts, thus relying upon intensity as a single parameter for separating desired signals from the background. The sole reliance on intensity for studying condensate-enriched proteins is suboptimal because the dilute fraction of fluorescently labeled condensate proteins elevates the amplitude of background signals, thus decreasing signal-to-noise ratios. Fluorescence lifetime imaging microscopy (FLIM) measures fluorescence with two parameters: intensity and fluorescence lifetime. Fluorescence lifetime is sensitive to changes in microenvironment, such as pH (Lin et al., 2003), ion and water density (Malacrida and Gratton, 2018; Mangiarotti et al., 2023), and the proximity of acceptor molecules suitable

[1]Department of Molecular and Cellular Biology, Baylor College of Medicine, Houston, TX, USA; [2]Dan L. Duncan Comprehensive Cancer Center, Baylor College of Medicine, Houston, TX, USA; [3]Molecular Microscopy and Spectroscopy, Istituto Italiano di Tecnologia, Genoa, Italy; [4]FLIM LABS S.r.l., Rome, Italy.

*L.E. Fahim and J.M. Marcus contributed equally to this paper; Correspondence to Jason E. Lee: jason.lee2@bcm.edu

**L.E. Fahim and J.M. Marcus are co-first authors.

for Förster resonance energy transfer (FRET) (Chen et al., 2003; Hinde et al., 2012). Two recent studies also detected fluorescence lifetime shifts when fluorescent proteins were fused to factors enriched in nuclear condensates (Pliss et al., 2019) and stress granules (Perego et al., 2023), thus making fluorescence lifetime a promising parameter to exploit for condensate studies. Additionally, FLIM provides investigators with additional signal processing approaches to potentially distinguish condensed and dilute phases independent of fluorescence intensity, such as phasor plot analyses (Weber, 1981; Digman et al., 2008; Malacrida et al., 2021).

FLIM excites samples with a pulsed light source to capture time-correlated-single-photon-counting (TCSPC) histogram data and generate fluorescence decay curves for each pixel. Pixels are moved from the time domain to frequency domain by performing a Fourier transform on fluorescence decay curves to yield G and S phasor coordinates, such that pixels with similar fluorescence lifetimes cluster together on a phasor plot (Fig. 1 A). Pixel clusters on a phasor plot can be segmented to provide a threshold-independent approach for resolving desired signals from undesired signals, such as spectral bleed-through, autofluorescence, and light source noise (Digman et al., 2008; Malacrida et al., 2021). Here, we evaluated the relationship between fluorescence lifetime and condensates by analyzing TCSPC FLIM data of fluorescently tagged proteins that localized to either stress granules or P-bodies. The detection of condensate-specific fluorescence lifetime signatures provided the basis for developing phasor plot-based approaches to isolate condensate pixels with the purpose of resolving key proteinprotein interactions within condensates using FLIM-FRET.

Results

Resolving stress granule and dilute phase signals by fluorescence lifetime

Stress granules are non-spontaneous RNP condensates that are absent under basal conditions and form within minutes of exposure to oxidative stress (Sanders et al., 2020; Kedersha et al., 1999). The inducible property of stress granules provides ideal experimental conditions to evaluate the sensitivity of fluorescent proteins in condensate microenvironments. Human osteosarcoma (U-2 OS) cells stably expressing monomeric NeonGreen (mNG) fused to a core stress granule protein, Ras GTPase-activating protein-binding protein 1 (mNG-G3BP1), were captured using FLIM before and during the oxidative stress response. As expected, fluorescence intensity images showed cells reorganizing mNG-G3BP1 from a diffuse dilute phase to a mix of stress granules and a dilute phase after the addition of sodium arsenite ($NaAsO_2$) (Fig. 1 B). Since unstressed cells displayed no detectable stress granules, we compared mNG-G3BP1 mean fluorescence lifetimes from the dilute phase of unstressed cells to stress granules of stressed cells. A traditional organelle segmentation algorithm using background subtraction (Otsu, 1979; Bray and Carpenter, 2018), referred to herein as intensity-threshold segmentation, was used to generate a stress granule mask and obtain stress granule-localized fluorescence lifetime histograms (Fig. 1 C).

The fluorescence lifetimes of mNG excited inside stress granules were longer than the lifetimes of signals emitted from the dilute phase of unstressed cells (Fig. 1 and Fig. S1). Notably, we observed similar changes in stress granule–localized fluorescence lifetime with an enhanced green fluorescent protein (G3BP1-eGFP) when analyzing data captured from a different FLIM system (Perego et al., 2023; Rossetta et al., 2022) (Fig. S2). Detectable fluorescence lifetime differences between stress granules and dilute phase suggest that condensate-localized pixels have fluorescence lifetime signatures, which can be exploited for a broad range of condensate-relevant analyses, such as calculating condensate size and abundance or tracking condensate-enriched interactions.

We further tested whether fluorescence lifetime can be used to distinguish condensate microenvironments from dilute phase by artificially recruiting a non-stress granule resident protein to stress granules using rapamycin-inducible FKBP and FRB (Fujisawa Kaihatsu-506 binding protein and FKBP-rapamycin binding protein) dimerization domains (Csordás et al., 2010) (Fig. 1 E). U-2 OS cells stably co-expressing mTurquoise2 (mTQ2)-G3BP1-FKBP and valosin-containing protein (mNG-VCP-FRB) were first exposed to oxidative stress to form stress granules, then FLIM images were captured before and after a 10-min rapamycin treatment (Fig. 1 F). The rapid recruitment of VCP to stress granules induced a shift in mNG-VCP-FRB fluorescence lifetimes (Fig. 1 G). Taken together, these data demonstrate the potential of using fluorescence lifetime to isolate condensate pixels for particle and time-lapse FLIM-FRET analyses, which enables the visualization of protein–protein interaction network dynamics within RNP condensates.

Phasor plot filtering approaches to distinguish RNP condensates from the dilute phase

Organelle segmentation by intensity-threshold segmentation remains challenging for organelles with a broad range of fluorescence intensities, such as the endoplasmic reticulum (ER) (Fig. S3), or small condensates, such as P-bodies or nuclear speckles. Moreover, intensity-threshold segmentation is particularly inefficient at parsing desired from undesired signals in tissue samples with high background, or when studying condensate proteins with weak phase separation, which yields a bright dilute phase (Riback et al., 2020). Phasor plots cluster pixels with similar fluorescence lifetimes and spatially separate pixels with different lifetimes, thus providing the potential to sort condensate pixels from dilute phase pixels without background subtraction. Here, we tested whether phasor plots can resolve stress granule–specific fluorescence lifetime shifts to generate condensate masks for particle and lifetime analyses (Fig. 2). Unfiltered phasor coordinates from mNG-G3BP1 and G3BP1-eGFP FLIM data (Perego et al., 2023) displayed a single cluster on phasor plots, which was not amenable for stress granule segmentation (Fig. S2 C and Fig. S4 A). Since signal processing and filtering of phasor coordinates have both been shown to improve lifetime cluster separation on phasor plots (Digman et al., 2008; Wang et al., 2021), we tested the effectiveness of median- and wavelet-filtered phasor coordinates for

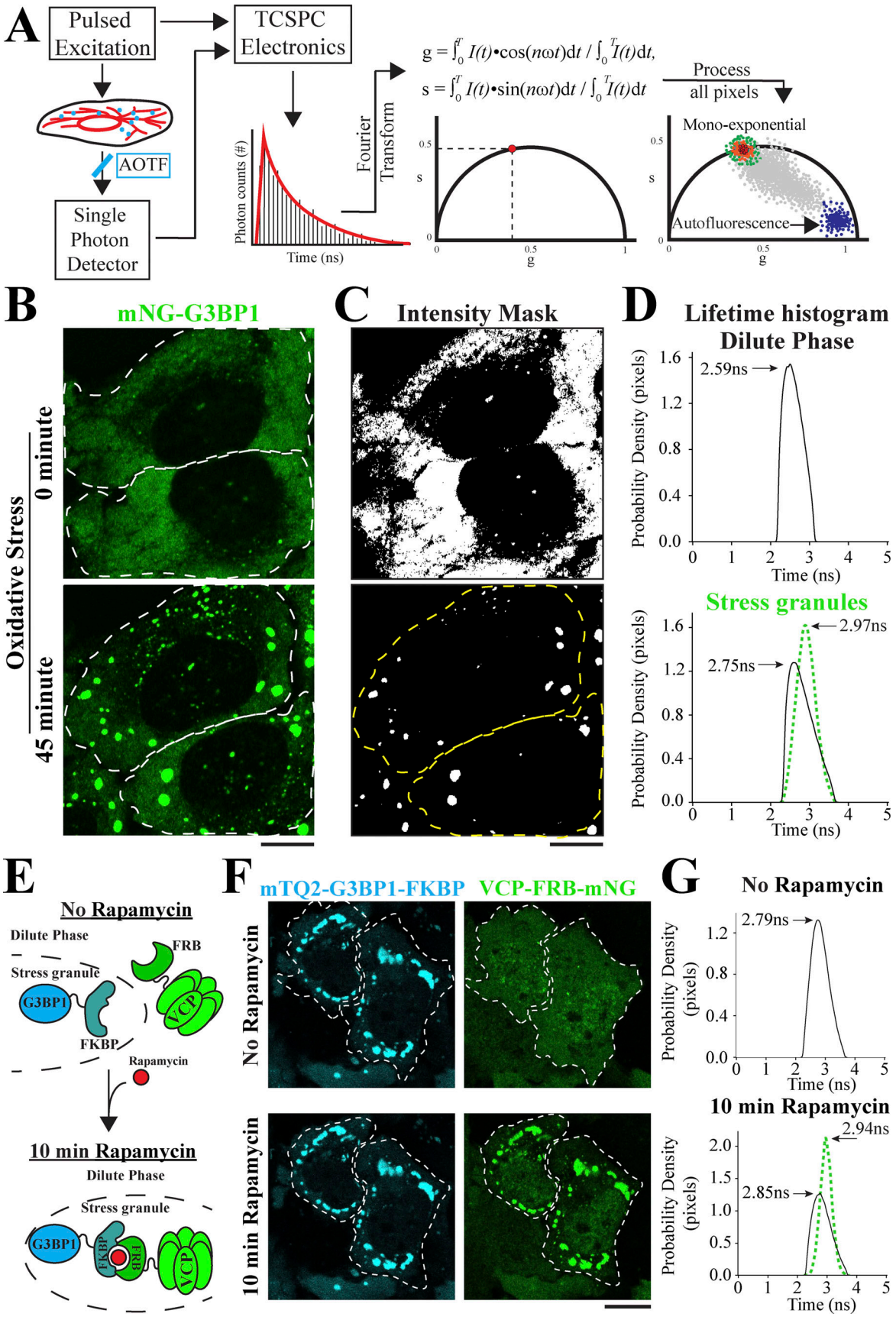

Figure 1. **FLIM of stress granules reveal fluorescence lifetime differences between condensed and dilute phases. (A)** A schematic for time-domain FLIM data capture using Acousto-Optic Tunable Filters (AOTF) followed by transformation to frequency-domain for pixel distribution on phasor plots. The TCSPC

profile (red curve) represents the I(t) function used in the integral formulas. Fluorescence lifetimes on phasor plots move from longer to shorter times in a clockwise direction. **(B)** Fluorescence intensity images from tile-scan time-lapses of U-2 OS cells stably expressing mNG-G3BP1 (stress granule marker) before and after a 45-min treatment with 0.5 mM $NaAsO_2$. **(C and D)** Intensity-threshold masks of the dilute phase (top) and stress granules (bottom) are generated by Cell Profiler (Bray and Carpenter, 2018). The pixels within the two masks were used to generate mNG fluorescence lifetime histograms for dilute phase (solid) and stress granules (dashed green). **(E)** Cartoon representation of the rapamycin-inducible FKBP and FRB dimerization system used to recruit VCP-FRB-mNG to mTQ2-G3BP1-FKBP–enriched stress granules. **(F)** U-2 OS cells stably co-expressing VCP-FRB-mNG (green) and mTQ2-G3BP1-FKBP (cyan) were treated with 0.5 mM $NaAsO_2$ for 45 min to induce stress granule formation prior to imaging. Tile-scan time-lapse images were captured before and 10 min after the addition of 200 nM rapamycin to recruit VCP to stress granules. Displayed are fluorescence-intensity images cropped from tile-scan mosaics. **(G)** Fluorescence-lifetime histograms of VCP-FRB-mNG within stress granules (dashed green) and dilute phase (solid) were obtained before and after treatment with rapamycin. Dashed lines demarcate cell boundaries. *N* = 3 biological replicates for experiments in B–D (*n* = 60 cells) and E–G (*n* = 15 cells). Scale bars = 10 µm.

separating stress granule and dilute phase fluorescence lifetime clusters (Fig. 2 A; Fig. S2, D and E; and Fig. S4, A and B).

We used open-source, Python-based software to transform TCSPC data into unfiltered and median-filtered phasor coordinates (Gottlieb et al., 2023). A previous study combined a dual-tree complex wavelet filter with an Anscombe transform to improve the resolution of FLIM data captured from samples with low signal-to-noise (Wang et al., 2021). Thus, we developed a Python-based wavelet filter optimized for resolving condensates from the dilute phase on phasor plots to process unfiltered phasor coordinates into wavelet-filtered coordinates. Under basal conditions, mNG-G3BP1 signals were enriched within a single dilute phase lifetime cluster on all phasor plots (Fig. 2 A; and Fig. S4, A and B, top panels). Strikingly, after cells were exposed to oxidative stress, phasor plots with median- and wavelet-filtered phasor coordinates revealed two distinct mNG-G3BP1 lifetime clusters (Fig. 2 A and Fig. S4 B, bottom panels). Importantly, analogous FLIM data captured from oxidative stress-exposed cells expressing G3BP1-eGFP on a different FLIM system responded similarly to median and wavelet filtering (Fig. S2, D and E).

These data show that stress granule pixels can be distinguished from dilute phase pixels on filtered phasor plots, thus demonstrating the feasibility of using filtered phasor plots to segment condensates without signal subtraction. Furthermore, the wavelet filter outperforms the median filter by retaining spatial resolution in time domain and by increasing stress granule lifetime cluster separation in the frequency domain (Fig. 2 A compared to Fig. S4 B). Thus, we focused herein on optimizing phasor plot segmentation using the wavelet filter.

Unsupervised machine-learning phasor plot segmentation outperforms classical intensity-threshold segmentation for distinguishing RNP condensates from the dilute phase

Next, we evaluated whether wavelet-filtered phasor plots are capable of sensing and sorting P-body pixels, which are significantly smaller condensates than stress granules. P-bodies are evolutionarily conserved RNP condensates that are present under basal conditions and responsive to oxidative stress. Time-lapse FLIM images were captured in human alveolar basal epithelial (A549) cells stably expressing the core P-body protein, mNG-DDX6 (dead-box helicase 6), before and during oxidative stress (Fig. 2 B). TCSPC data were used to generate wavelet-filtered phasor plots (Fig. 2 C). DDX6-marked P-body phasor plots displayed multiple lifetime clusters like stress granule phasor plots. Strikingly, P-body pixels displayed a larger separation from dilute phase pixels on phasor plots compared to stress granules, which could reflect differences in the partitioning of G3BP1 and DDX6, or a difference in the photo-physics of mNG when tagging different proteins (Fig. 2 C).

Manual phasor plot segmentation is subjective, time-consuming, and inaccessible to most FLIM systems. Therefore, we developed an unsupervised machine-learning approach to segment condensate lifetime clusters on wavelet-filtered phasor plots using Gaussian mixture modeling (GMM) (Vallmitjana et al., 2021), which analyzes covariance to identify gaussian centers within spatially distributed data. Thus, we used GMM calculated covariances around the center coordinates of the condensate cluster to define region of interest (ROI) size. Additionally, most stress granule factors display weaker partitioning compared with many P-body proteins (Sanders et al., 2020). Here, we show that differences in partitioning strengths appear to be proportional to the distances between the condensed and dilute phase lifetime clusters (Fig. 2 D). We exploited the separation between condensed and dilute phase clusters to optimize ROI size, such that stress granules labeled with mNG-G3BP1 and P-bodies labeled with mNG-DDX6 were efficiently segmented on phasor plots with elliptical ROI sizes determined by 2.5 and 3.0 times the covariance, respectively. The segmentation of wavelet-filtered phasor plots produced stress granule and P-body masks, which precisely captured pixels within condensates of a wide range of size and brightness (Fig. 3, A and D; and Fig. S2 E).

Next, the performance of phasor plot segmentation was evaluated by calculating the extent of overlap between intensity-threshold-generated masks of stress granules and P-bodies (Fig. 1 C, bottom, and Fig. 3 E) and their respective wavelet-phasor plot masks (Fig. 3, A and D). Scatterplot analysis of mask overlap as a function of stress granule area reveals that phasor plot segmentation matches the performance of intensity-threshold segmentation for larger structures and significantly outperforms for smaller structures (Fig. 3, B and C). For P-bodies, phasor plot segmentation significantly outperforms intensity-threshold segmentation for quantifying both P-body size and abundance (Fig. 3 E). Together, these experiments demonstrate the utility and precision of phasor plot filtering and automated segmentation to precisely distinguish RNP condensates from their respective dilute phases across multiple FLIM systems.

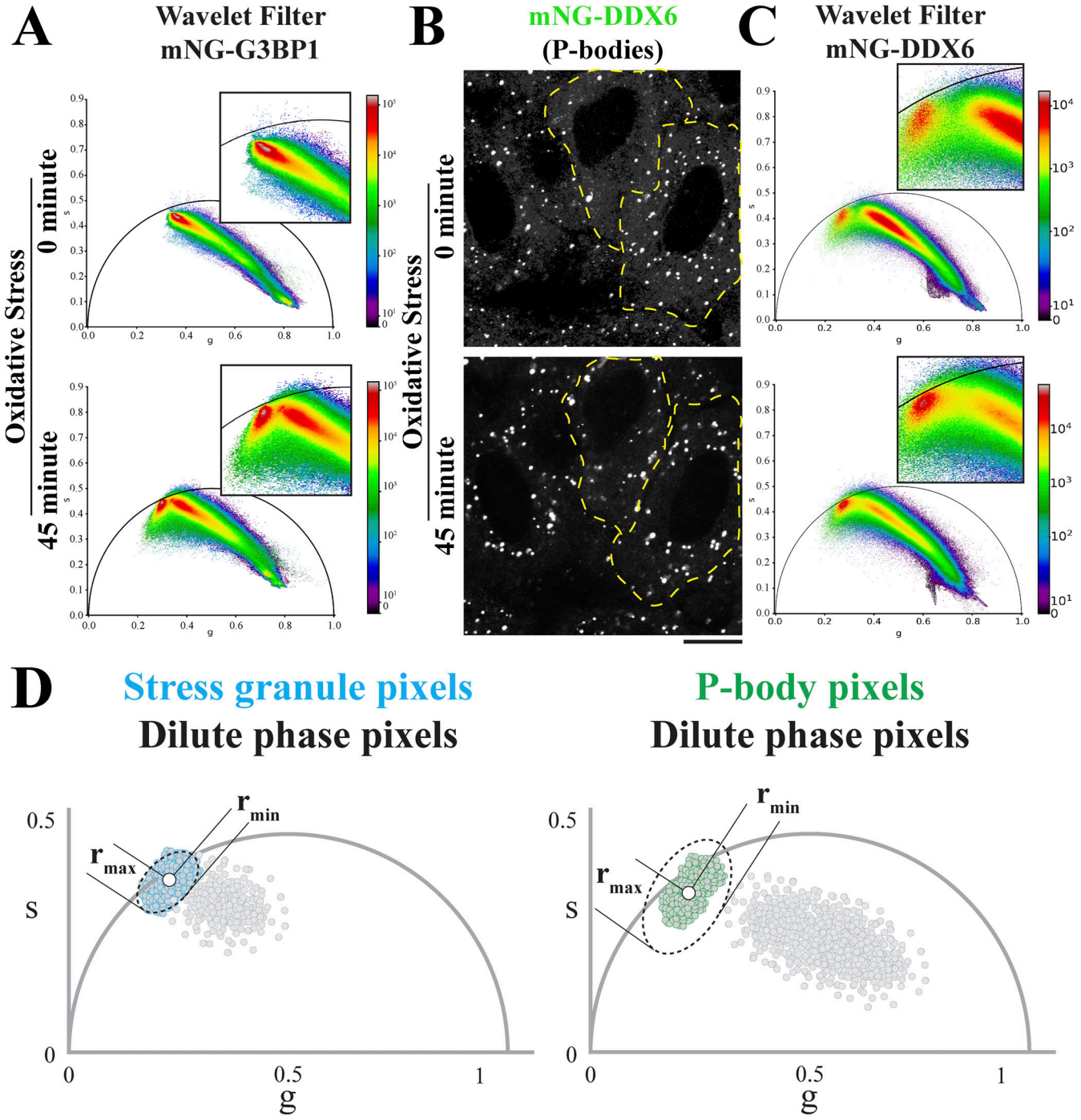

Figure 2. **The condensed and dilute phases of RNP condensates are resolvable on wavelet-filtered phasor plots with machine-learning algorithms. (A)** Unthresholded, wavelet-filtered phasor plots of all pixels accumulated from tile-scan images from Fig. 1 B expressing mNG-G3BP1 before (top) and during oxidative stress (bottom). Note the appearance of a stress granule cluster during oxidative stress (bottom). Insets highlight the absence and presence of a stress granule lifetime cluster before and during stress, respectively. **(B and C)** Fluorescence intensity images of mNG-DDX6–marked P-bodies and dilute phase in A549 cells before (top) and during oxidative stress (bottom), and their corresponding unthresholded, wavelet-filtered phasor plots. Insets highlight the presence of P-body lifetime clusters before and during stress. Note the increase in density of the P-body lifetime clusters during stress, and the corresponding decrease in dilute phase density corresponding to stress-induced P-body biogenesis and increased partitioning (bottom phasor plot). Scale bars = 10 µm. **(D)** Cartoon of phasor plots illustrating the relationships between ROI, covariance, and the strength of partitioning. The size and shape of the ROI are determined by the covariance of the condensate cluster. *n* = 60 and 91 cells in mNG-G3BP1 and mNG-DDX6 expressing conditions across three biological replicates, respectively.

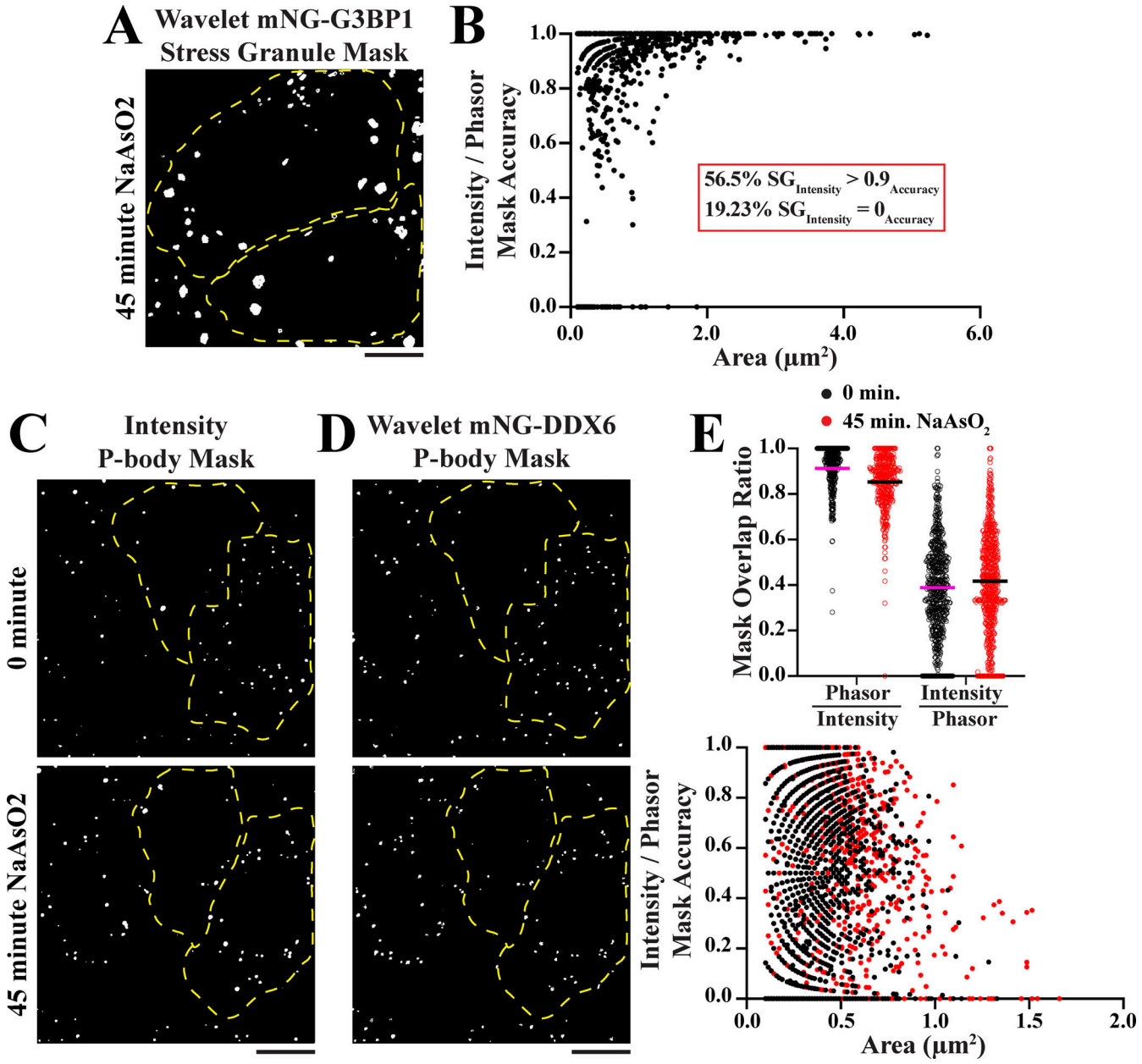

Figure 3. **Automated segmentation of wavelet-filtered phasor plots generates RNP condensate masks, which outperform intensity-threshold-based segmentation for accurately detecting smaller condensates. (A)** A stress granule mask generated from GMM-covariance-guided segmentation of wavelet-filtered phasor plots from Fig. 2 A (bottom) corresponding to cells from Fig. 1 B. **(B)** Intensity-threshold stress granule masks from Fig. 1 C were overlayed on phasor masks from A to assess their degree of overlap. Phasor masks outperformed intensity-threshold masks for smaller stress granules (<2 µm²). **(C and D)** Intensity-threshold and phasor P-body masks from mNG-DDX6–expressing cells in Fig. 2 B. **(E)** Phasor P-body masks were overlayed on intensity-threshold masks, and vice versa, to assess their degree of overlap. Phasor-derived P-body masks outperformed intensity-threshold masks for assessing size and number. Dashed lines demarcate cell boundaries. Scale bars = 10 µm. *N* = 3 biological replicates, *n* = 91 cells.

Developing an automated condensate-specific FLIM-FRET approach by evaluating core protein interactions within P-bodies and stress granules

The ability to resolve RNP condensates by two parameters, intensity and fluorescence lifetime, provides a foundation for developing condensate-specific FLIM-FRET assays. Briefly, FLIM-FRET is calculated by measuring the extent of donor lifetime shortening, which is a function of the distance between donor and acceptor fluorophores (Malacrida et al., 2021; Chen et al., 2003) (Fig. 4 A). A major advantage of a donor FRET readout compared with the acceptor readout of classic FRET is that FLIM-FRET assays can be centered around donor fluorophores engineered to be bright, photostable, and monomeric, such as mNG (Shaner et al., 2013; Heim and Tsien, 1996). Additionally, FLIM-FRET is not affected by spectral bleed-through, which enables the use of efficient FRET acceptors while circumventing the impact of direct acceptor excitation with donor excitation laser pulses. Here, we describe an automated condensate FLIM-FRET analysis pipeline

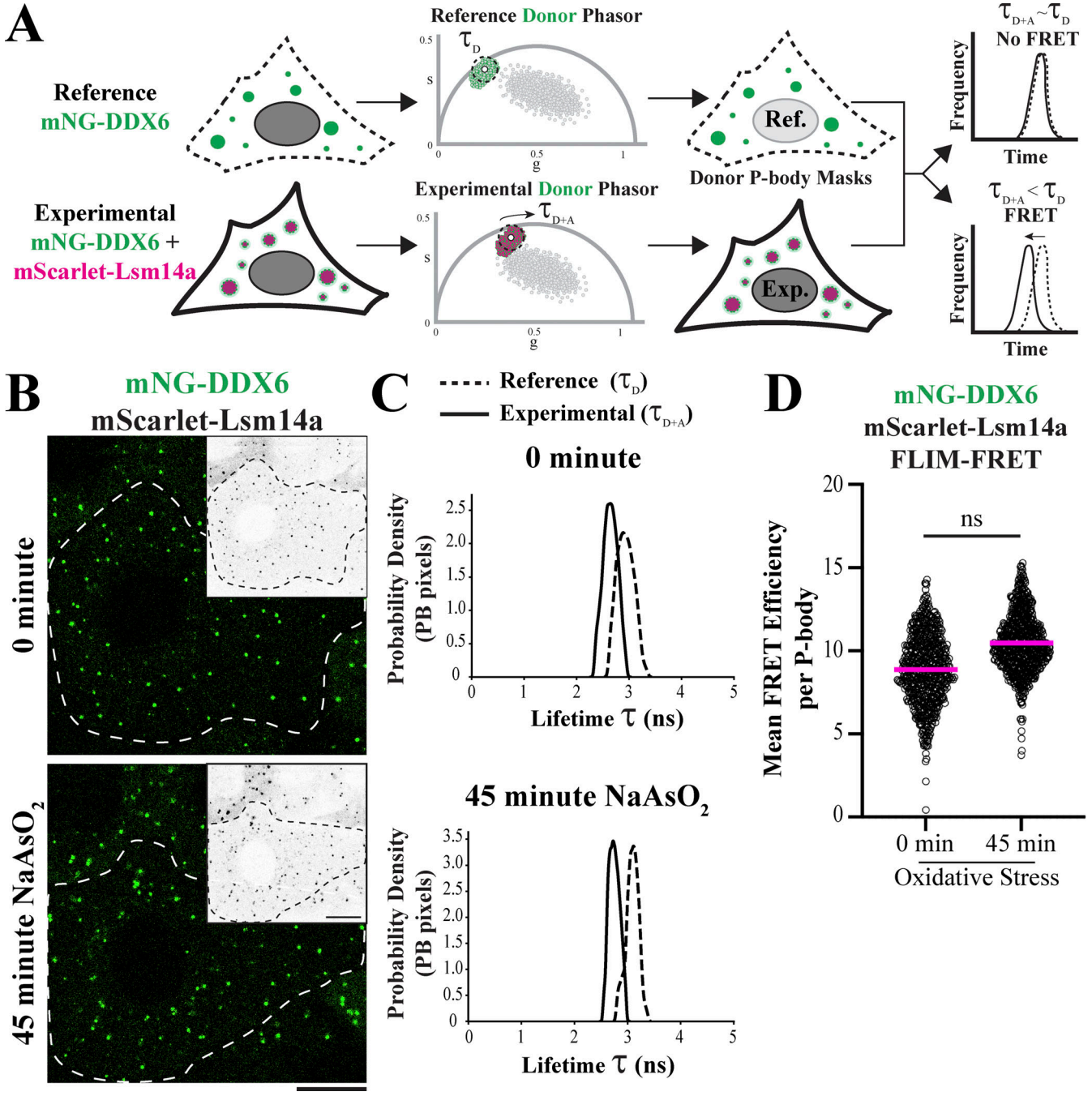

Figure 4. **Automated condensate FLIM-FRET enables live tracking of protein–protein interactions within P-bodies across many cells through $NaAsO_2$ treatment. (A)** Cartoon schematic of a two-cell line approach to evaluate mNG-DDX6 donor lifetimes in reference (Ref.) and experimental (Exp.) cells for the quantification of mean FRET efficiency within P-bodies. A clockwise rotation of the experimental donor lifetime cluster represents shorter lifetimes resulting from FRET. **(B)** Fluorescence intensity images of experimental A549 cells stably expressing mNG-DDX6 and mScarlet-Lsm14a. The reference cells displayed in Fig. 2 C were captured on the same day as the experimental cells. Scale bars = 10 µm. **(C)** Fluorescence lifetime kernel density plots of condensate-specific mNG-DDX6 pixels from reference (dashed) and experimental (solid) cells. **(D)** FLIM-FRET efficiencies of individual P-bodies before and during stress were calculated by using the mean fluorescence lifetimes of reference P-bodies (τ_D) and individual experimental P-bodies (τ_{nD+A}) in the formula, $E_{FRET} = 100 \cdot [1-(\tau_{nD+A}/\tau_D)]$, such that [*n*] = the total number of P-bodies. The magenta line represents the mean of individual P-body FLIM-FRET efficiencies. Statistical significance was determined by nested *T* test, ns = not significant. *N* = 3 biological replicates, *n* = 179 cells.

founded on the ability to extract condensate-specific pixels from wavelet-filtered phasor plots. Moreover, we outline two experimental approaches using two different classes of acceptor fluorophores to increase accessibility and rigor.

The basis for condensate FLIM-FRET relies on reference cells, which only emit donor fluorescence, and experimental cells capable of emitting donor and acceptor fluorescence. Donor TCSPC data from reference and experimental cells are processed

to generate wavelet-filtered phasor plots, which are then segmented to sort condensate-specific pixels and generate donor condensate masks from the two cell lines (Fig. 4 A). Reference and experimental condensate masks are then used to compile reference and experimental lifetime histograms to calculate mean FRET efficiency (Clegg, 1995) with single condensate resolution.

To demonstrate the feasibility of condensate FLIM-FRET, we evaluated known interactions between DDX6 and Lsm14a in P-bodies, and G3BP1 homodimers in stress granules (Sanders et al., 2020; Brandmann et al., 2018). P-body–localized fluorescence lifetimes were calculated from A549 reference cells expressing mNG-DDX6 (donor) (Fig. 3 A) and from A549 experimental cells co-expressing mNG-DDX6 and mScarlet-Lsm14a (acceptor) (Fig. 4 B). The two cell lines were captured with FLIM on the same day using identical capture and stress-inducing conditions. P-body–specific lifetime histograms (Fig. 4 C) and mean FRET efficiencies of individual P-bodies (Fig. 4 D) revealed FRET efficiencies of 9.0% and 10.4% before and during stress, respectively. A similar FRET efficiency (11.3%) was observed in stress granules with dimers consisting of mNG-G3BP1 and mScarlet-G3BP1 (Fig. S5). Together, condensate FLIM-FRET analyses of core protein interactions within stress granules and P-bodies provide a benchmark for interpreting the significance of FRET efficiency measurements between dynamic and potentially tunable interactions.

Condensate FLIM-FRET reveals dynamic interactions within mRNA P-bodies

The regulated assembly of biomolecular complexes constitutes a fundamental cellular mechanism for dictating where and when cellular processes occur. P-bodies enrich for enzyme complexes that drive mRNA decapping and decay (Jonas and Izaurralde, 2013; Chang et al., 2014; Tibble et al., 2021), mRNA silencing (Schirle et al., 2014), and mRNA editing (Cho et al., 2003). However, a major question is whether P-bodies concentrate mRNA decay factors to inhibit or to facilitate their assembly. RNA sequencing performed on P-bodies isolated by fluorescence particle sorting identified largely intact transcripts (Hubstenberger et al., 2017), thus supporting a P-body model of mRNA sequestration and an inhibition of mRNA decay. Conversely, purified subunits of the yeast mRNA decapping complex, Dcp2, Dcp1, and EDC3 (enhancer of decapping 3) readily formed condensates in vitro to increase decapping rates of mRNA substrates suggesting P-bodies might enrich mRNA decapping complex subunits to enhance Dcp2 enzyme function (Tibble et al., 2021). However, both approaches were conducted outside of a live cellular environment (Tibble et al., 2021; Hubstenberger et al., 2017). Therefore, we used condensate FLIM-FRET to determine whether key subunit interactions of the human mRNA decapping complex occur within P-bodies.

Using mNG and mScarlet as FRET pairs, we evaluated interactions between Dcp2-Dcp1A, Dcp2-EDC3, and EDC3-Dcp1A in A549 cells (Fig. S6). Under basal conditions, P-body–enriched Dcp2-Dcp1A and EDC3-Dcp1A yielded FRET efficiencies of 8.5% and 9.9%, respectively (Fig. S6), which are in line with DDX6-Lsm14a FRET efficiency calculations (Fig. 4 D). Dcp2-EDC3 yielded a significantly lower FRET efficiency (3.3%), which suggests EDC3 might primarily interact with Dcp1A and not Dcp2 in humans. After 45 min of oxidative stress, Dcp1A-EDC3 FRET remains unchanged, whereas FRET efficiency between Dcp2-Dcp1A and Dcp2-EDC3 drops to 2.8% and 1.8%, respectively. These data reveal context-dependent plasticity of the mRNA decapping complex within human P-bodies, whereby Dcp2 and Dcp1A interactions are reduced during stress despite their co-enrichment with P-bodies. Additionally, human Dcp1A stably interacts with EDC3 and Dcp2 only under basal conditions (Fig. S6), which is contrary to yeast where yeast Dcp2 has been shown to interact with Dcp1 and EDC3 (Charenton et al., 2016). Thus, our P-body FLIM-FRET data of the human decapping complex supports a model, which attributes differences between yeast and human decapping complex interactions to the transfer of a long intrinsically disordered region (IDR) from yeast Dcp2 to human Dcp1A/Dcp1B (Jonas and Izaurralde, 2013).

Technically, the dual cell line approach is an efficient and cost-effective approach for FLIM-FRET experiments, especially if expression constructs for candidate proteins fused to FRET pairs already exist. It is important to note that using two cell lines will have intrinsically different condensate compositions because reference cell lines only express mNG-tagged condensate proteins, whereas experimental cell lines express mNG- and mScarlet-tagged proteins. Below, we describe a condensate FLIM-FRET approach, which relies on a single cell line to report reference and experimental lifetimes from condensates with intrinsically identical compositions (Fig. 5 A).

Elucidating Dcp2 and Dcp1A interaction dynamics with condensate FLIM-FRET using cell-permeable acceptor dyes

The compositional and material properties of biomolecular condensates can be sensitive to changes in condensate factor expression, as well as the expression of certain fluorescent proteins, such as green and red fluorescent protein (GFP, RFP) (Currie et al., 2023; Barkley et al., 2024). HaloTag and mNG displayed the best performance for studying viral condensates because cells expressing Halo-, mNG-tagged, or untagged viral proteins yielded condensates with similar size, shape, number, and diffusion rates (Barkley et al., 2024). Thus, we aimed to overcome two technical challenges of the mNG-mScarlet FLIM-FRET pair by replacing mScarlet with HaloTag (Fig. 5 A). First, potential condensate artifacts associated with expressing an RFP (mScarlet) are circumvented. Second, compositional and material differences between reference and experimental condensates assayed from different cell lines are avoided by developing a single-cell line approach to capture reference and experimental condensate lifetimes. Here, we tested a commercially available, cell-permeable dye (JaneliaFluor JF549), which, when conjugated to Halo, has a predicted Förster radius (R_o) of 58.65Å with mNG (Lambert, 2019).

To evaluate the validity of a mNG-HaloTag FLIM-FRET approach, we stably expressed mNG-Dcp2 in *DCP1A/DCP1B* double knockout (*1A/1B* DKO) U-2 OS cells (Fig. S7) and acutely transduced the expression of either Halo-Dcp1A or Halo-DDX6. Reference and experimental FLIM images of mNG-Dcp2 and HaloTag-expressing *1A/1B* DKO cells were captured prior to and 30 min after JF549

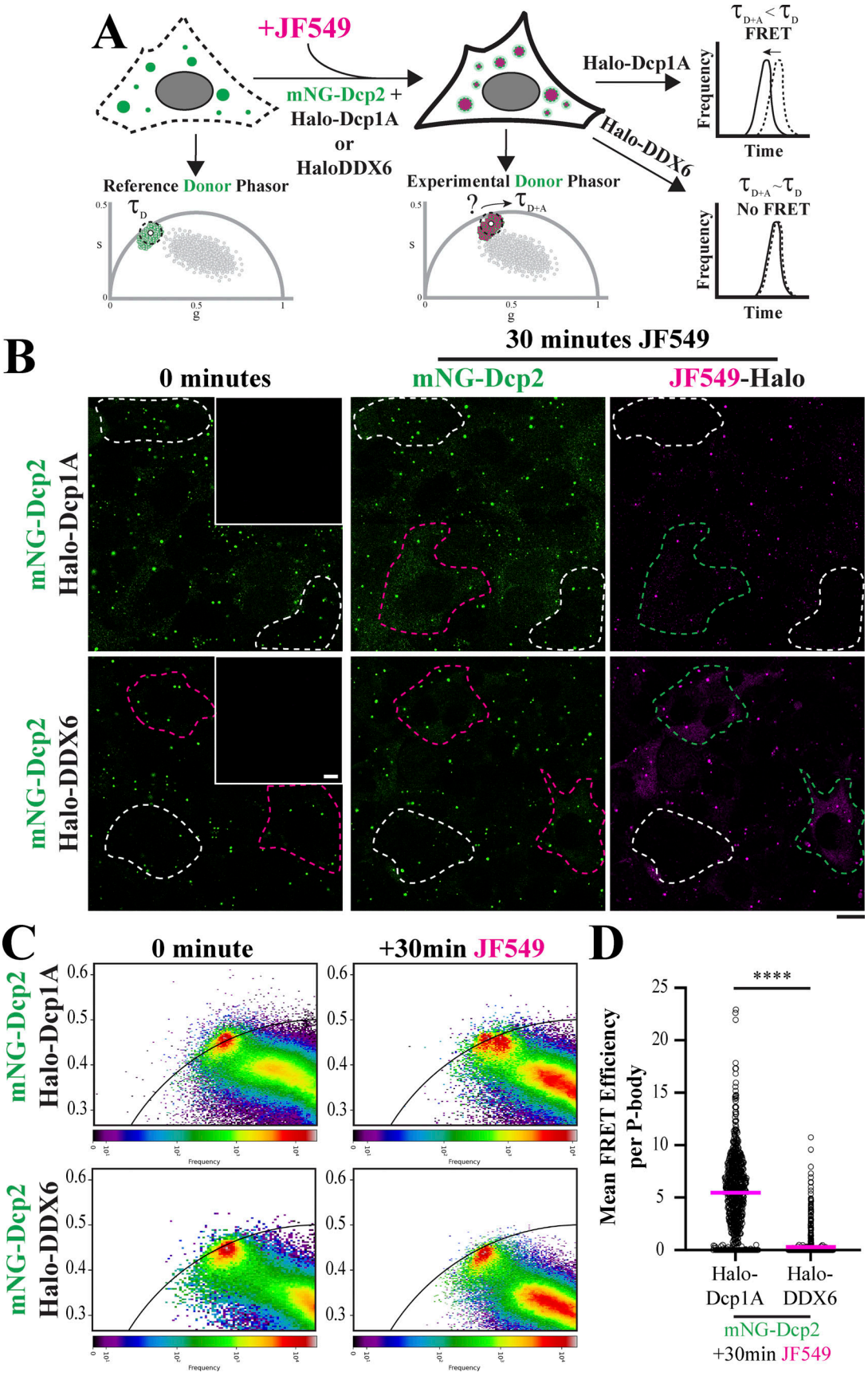

Figure 5. **A condensate FLIM-FRET approach utilizing cell-permeable dyes to capture reference and experimental measurements from P-bodies of similar molecular composition or from the same cells. (A)** Cartoon schematic of obtaining phasor plots from *DCP1A/1B* DKO cells stably expressing mNG-

Dcp2 and either Halo-Dcp1A or Halo-DDX6 before and after the addition of the JaneliaFluor (JF)549 acceptor dye. **(B)** Representative fluorescence intensity tile-scan time-lapse images before and after JF549 addition. The insets in the 0-min panels demonstrate the absence of fluorescence when the cells were excited with a 549 nm laser. Note the cells expressing (magenta/green boundaries) and not expressing (white boundaries) Halo-markers. Scale bar = 10 µm. **(C)** Unthresholded, wavelet-filtered phasor plots of mNG-Dcp2 captured from panel B. **(D)** Mean FLIM-FRET efficiencies of individual P-bodies from cells in panel B. Note that non-Halo– and Halo-DDX6–expressing cells yield ∼0% FRET efficiencies, thus demonstrating the sensitivity of condensate FLIM-FRET. Statistical significance was determined by nested *T* test. ****P < 0.00001. *n* = 133 and 109 cells in Halo-Dcp1A– and Halo-DDX6-–expressing conditions across three biological replicates, respectively.

addition to the cell culture media, respectively (Fig. 5 B). At 0 min, Halo-Dcp1A– and Halo-DDX6–expressing cells displayed a single mNG-Dcp2 lifetime cluster (Fig. 5 C: left phasor plot). Strikingly, after 30 min of JF549, only cells expressing Halo-Dcp1A yielded a decrease in mNG-Dcp2 fluorescence lifetimes (Fig. 5 C: top-right phasor plot). Furthermore, JF549 labeled a subset of cells to reveal HaloTag expressors (magenta/green boundaries) and non-HaloTag expressors (white boundaries) (Fig. 5 B). The two subpopulations of cells from the Halo-Dcp1A condition were reflected by two distinct P-body lifetime clusters on phasor plots (Fig. 5 C) and P-bodies with ∼0% and ∼7% mean FRET efficiencies (Fig. 5 D). Dcp2 and DDX6 have not been reported to directly interact in humans, which is reflected on phasor plots and a near-zero percent mean P-body FRET efficiency (Fig. 5, C and D). Together, these data demonstrate the viability and sensitivity of using mNG and JF549-HaloTag as condensate FLIM-FRET pairs.

Condensate FLIM-FRET reveals Dcp2 and Dcp1A remain uncoupled during stress recovery

Mammalian cell lines re-engage bulk translation and disassemble stress granules within 1 to 2 h of stress recovery (Wheeler et al., 2016; Moon et al., 2019; Lee et al., 2020); therefore, we chose the 2-h timepoint to assess whether Dcp2-Dcp1A FRET returns to prestressed levels (Fig. 6 A). *1A/1B* DKO U-2 OS cells stably expressing mNG-Dcp2 and acutely expressing Halo-Dcp1A were assessed for condensate FLIM-FRET before stress, during stress, and after 2 h of stress recovery. Experimental P-body lifetime clusters displayed a clear FLIM-FRET shift on wavelet-filtered phasor plots under basal conditions and a movement closer to the reference cluster during stress, which corresponded to mean Dcp2-Dcp1A FRET efficiencies of 9.0% and 4.7% within P-bodies, respectively (Fig. 6, B and C). 2 h into stress recovery, experimental P-body lifetime clusters surprisingly maintained a tight overlap with reference clusters and reported mean Dcp2-Dcp1A FRET efficiencies of 3.0% within P-bodies, which suggests mRNA decapping remains suppressed even after the stressor was removed (Fig. 6, B and C).

To test whether the absence of Dcp2-Dcp1A FLIM-FRET during recovery was due to the loss of endogenous Dcp1B in *1A/1B* DKO U-2 OS cells or if the lack of Dcp2-Dcp1A FLIM-FRET recovery is cell-type specific, an analogous experiment was performed in A549 cells stably expressing mNG-Dcp2 and acutely expressing Halo-Dcp1A or Halo-DDX6. Cells co-expressing Halo-DDX6 yielded near-zero mean P-body FRET efficiencies for all treatment conditions (Fig. 6 D). Conversely, Halo-Dcp1A co-expressing cells registered mean P-body FRET efficiencies of 12.0%, 4.8%, and 4.3% under basal, stressed, and stress recovery conditions, respectively (Fig. 6 D). Collectively, these data demonstrate the tunability of a critical interaction for mRNA decapping under basal and stressed conditions. Furthermore, these data suggest that mRNA decapping activity lags behind the resumption of mRNA translation during stress recovery.

Potential to couple condensate FLIM-FRET with protein-folding algorithms

FRET detection is evaded when the orientation of two interacting proteins position donor and acceptor fluorophores beyond their Förster radius. Thus, any structural insight into how proteins interact can be useful for determining whether to place fluorophores on the N- or C-terminus. As protein structure prediction algorithms continue to advance, algorithms, such as AlphaFold (Abramson et al., 2024) and RoseTTAFold (Krishna et al., 2024), will become increasingly useful FLIM-FRET experimental design tools for predicting optimal donor and acceptor fluorophore placement. Below, we provide a conservative approach to using protein interaction structural maps generated by AlphaFold3 for predicting of the distance between donor and acceptor fluorophores, and for connecting our FLIM-FRET experimental results with AlphaFold3-calculated confidence levels using the predicted local distance difference test (pLDDT) (Mariani et al., 2013).

We modeled interactions between mNG-Dcp2 and Halo-Dcp1A using AlphaFold3 and measured a distance of 30.58 Å between the two fluorophores, which is within the Förster radius of mNG and JF549 (Fig. 7, A and B). Next, we cataloged potentially interacting atoms by their pLDDT confidence level. Atoms of two proteins are considered potential interactors or contacting when they are ≤4Å apart. Highlighted is a contact between high-confidence atoms of Dcp2 and Dcp1A with pLDDTs ≥0.9 (Fig. 7 A inset), which has been experimentally verified (Chang et al., 2014). Therefore, contacting atoms between Dcp2 and Dcp1A were binned and filtered between high (pLDDT ≥ 0.9 red), medium (pLDDT ≥ 0.7 white), and low (pLDDT ≥ 0.5 blue) confidence levels of atoms on both sides of the contact site. Dcp2-Dcp1A and Dcp1A-EDC3 interaction models yielded 21 and 27 high-confidence contacts, respectively (Fig. 7 C). Modeled interactions between the G3BP1 homodimer and DDX6-Lsm14a both showed the presence of high confidence contacts. Conversely, no high-confidence contacts were detected for Dcp2-EDC3 or Dcp2-DDX6 interaction models, such that the presence or absence of high-confidence contacts are consistent with our FLIM-FRET results (Fig. 7 C). Since many proteins enriched within condensates contain IDRs, the utility of protein structure algorithms for condensate FLIM-FRET will grow as algorithms improve their ability to predict the atomic positions of IDRs within complexes.

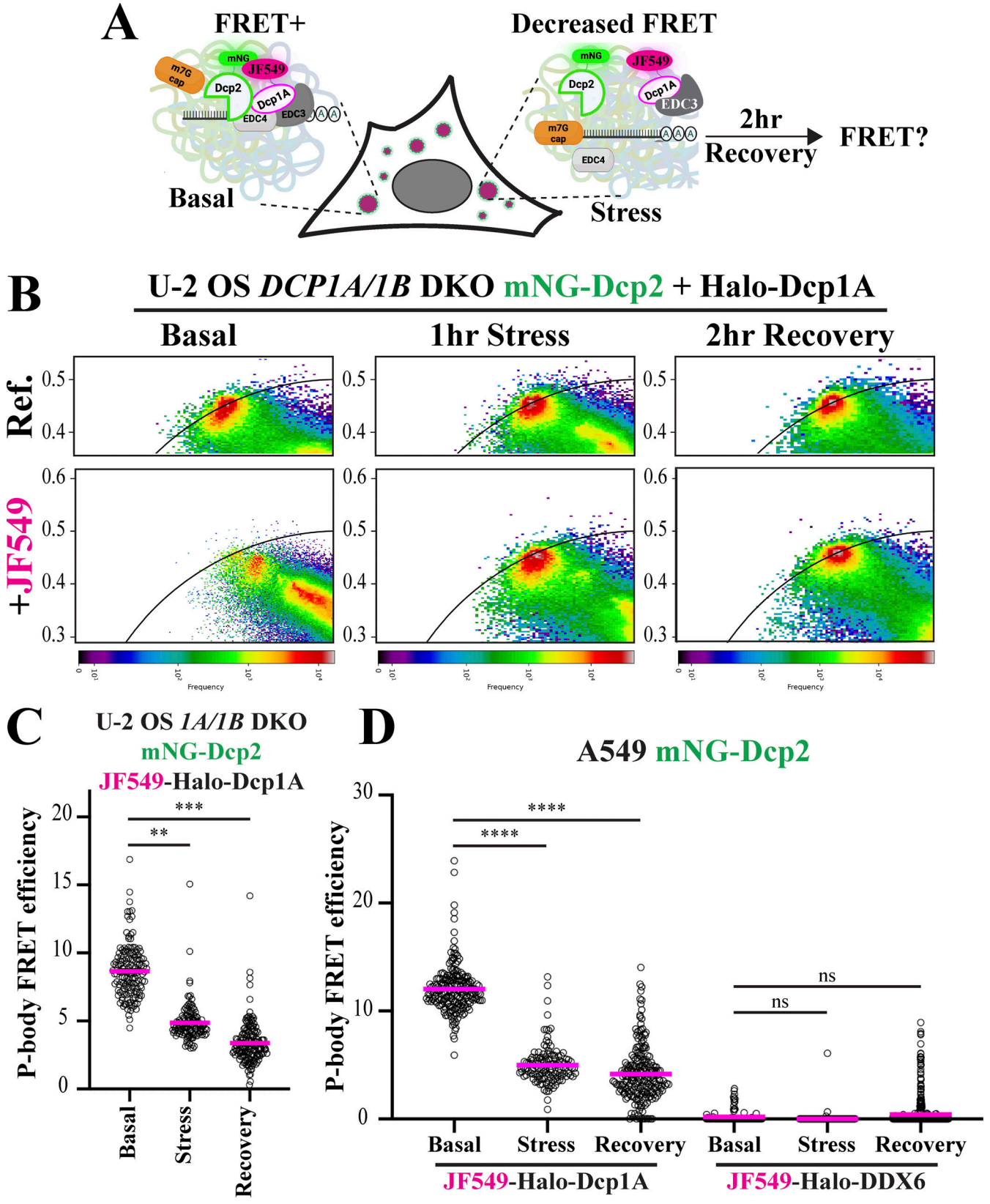

Figure 6. **The return of mRNA decapping complex FLIM-FRET is delayed during stress recovery. (A)** Cartoon schematic depicting mRNA decapping complex interaction dynamics before and during oxidative stress. **(B and C)** Unthresholded, wavelet-filtered phasor plots and mean FLIM-FRET efficiencies of mNG-Dcp2 and JF549-Halo-Dcp1A in individual P-bodies from *DCP1A/1B* DKO U-2 OS cells before, during, and after a 2-h washout of $NaAsO_2$, where n = 148, 132, 118 cells, respectively. **(D)** Condensate FLIM-FRET efficiencies performed in A549 cells co-expressing mNG-Dcp2 with either Halo-Dcp1A (n = 133, 119, 127 cells, respectively) or Halo-DDX6 (n = 108, 115, 89 cells, respectively) with a similar experimental layout to panel B. **(C and D)** Statistical significance was determined by nested one-way ANOVA. **P < 0.001, ***P < 0.0001, ****P < 0.00001. N = 3 biological replicates for all experiments.

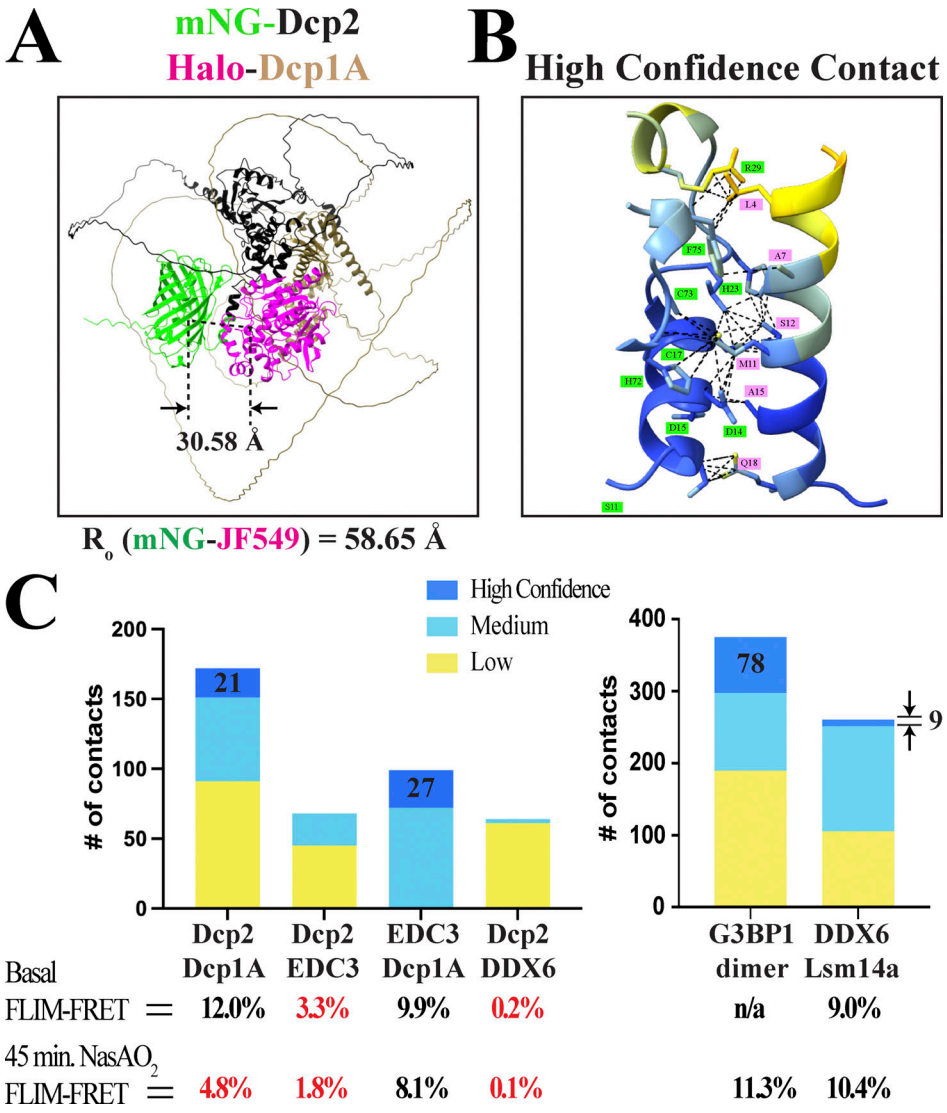

Figure 7. **The potential to combine condensate FLIM-FRET with computational protein structure and interaction algorithms for efficient validation of predicted models and for FLIM-FRET experimental design. (A)** AlphaFold3 model of mNG (green) fused to Dcp2 (black) and Halo (magenta) fused to Dcp1A (gold). The distance between the mNG chromophore and the Halo residue, which covalently binds compatible fluorophore dyes. Blue, cyan, and yellow correspond to high, medium, and low confidence atomic predictions. **(B)** A magnified view of a high confidence clash between Dcp2 and Dcp1A. **(C)** Quantifying the number of clashes with high (blue), medium (cyan), and low (yellow) confidence structural positions on both sides of the clash for the FRET pairs analyzed in this manuscript. Highlighted in red are low FRET efficiencies.

Discussion

Biomolecular condensates provide cells with the reflexes to acutely concentrate hundreds of molecules critical for cellular and organismal health within minutes in response to intrinsic and extrinsic stimuli. However, condensates remain a black box with respect to how their molecular networks are wired and dynamically regulated in different cellular contexts. This study reveals that subtle fluorescence lifetime differences between condensed and dilute phases can be exploited by phasor plot filtering to faithfully isolate condensate-specific pixels for rigorous FLIM-FRET analyses across tens to hundreds of cells. We used condensate FLIM-FRET to provide the first evidence that human mRNA decapping complex subunits interact within P-bodies. The tracking of P-body interactions under basal, stressed, and stress recovery conditions also revealed an unexpected layer of regulation, which converged on interactions between the mRNA decapping enzyme and a key coactivator. Our results raise new questions about how P-bodies and other condensates coordinate the assembly of enzyme complexes and re-ignites existing questions of whether complexes within P-bodies are catalytically active.

Short-read RNA-sequencing (RNA-seq) of P-body– or stress granule–enriched fractions has demonstrated that these condensates are sites of mRNA sequestration (Hubstenberger et al., 2017; Matheny et al., 2019). Our live-cell results and others (Blake et al., 2024) support the possibility that mRNA decay might occur in parallel to mRNA sequestration within P-bodies. Blake et al. developed a rapamycin-inducible non-sense mediated RNA decay (NMD) assay to show that P-bodies coalesce around RNA substrates upon recruitment of the NMD

machinery. P-body-localized NMD was attenuated during $NaAsO_2$-induced oxidative stress (Blake et al., 2024), which is consistent with our results showing that Dcp2-Dcp1A FRET was significantly decreased under the same stress condition. Consistent with *DCP2* knockdown studies in drosophila cells (Eulalio et al., 2007), inhibiting Dcp2 enzyme function by gene ablation of *DCP1A* and *DCP1B* in U-2 OS cells resulted in significant increases in P-body size and abundance (Fig. 6 and S7). Re-expression of Dcp1A took several days to restore P-body abundance to lower wild-type U-2 OS numbers suggesting that *DCP1A/1B* DKO cells are primed for P-body–localized RNA decay. Thus, short-read and true-end-to-end RNA-seq (Ibrahim et al., 2021) performed on P-bodies isolated from *DCP1A/1B* DKO cells with and without re-expression of Dcp1A would provide insight into which transcripts are accumulating within P-bodies from mRNA decapping-deficient cells, and whether transcript read densities in rescue cells will differ from published P-body–enriched transcriptomes, respectively.

Condensate FLIM-FRET provides the ability to connect descriptive live-cell studies of condensate dynamics with functional studies from reconstituted systems. Here, Dcp2 and Dcp1A were targeted because previous studies showed inhibition of decapping activity with immunoprecipitated human Dcp2 harboring mutations that disrupt Dcp1A binding (Chang et al., 2014). Our results from P-bodies in live cells showed decapping-critical interactions between Dcp2 and Dcp1A were present before stress but disrupted during stress, despite interactions between Dcp1A and EDC3 remaining stable under both conditions. The continued suppression of Dcp2 and Dcp1A interactions at a stress recovery timepoint where most cells have restarted bulk mRNA translation, suggests that the potential return of mRNA decapping might represent a decision checkpoint for cell survival or death. Moreover, EDC4/Hedls appears to be important for the interaction of Dcp2 with Dcp1A and other P-body–enriched enzymes (Fenger-Grøn et al., 2005; Brothers et al., 2023). Future condensate FLIM-FRET studies targeting the crosstalk between Dcp2, EDC4, and other RNA processing enzymes will help to elucidate the molecular switch controlling Dcp2 and Dcp1A interactions and shed light on the roles of enzyme complexes within P-bodies at different stages of the cell cycle, in different cell types, or under different types of stress.

Lastly, our wavelet-filtered, phasor plot segmentation workflow has been validated for processing TCSPC data from multiple FLIM systems, which will enable the rigorous use of a technology that is increasingly found in imaging core facilities around the world. More broadly, this study provides a blueprint to expand the use of FLIM phasor plots for resolving dilute phase FLIM-FRET, calculating protein partitioning between dilute and condensed phases, and tracking the dynamics of fluorescently labeled RNA and RNA–protein interactions within condensates. Furthermore, organelles perform multiple functions through the enrichment of different types of machinery and their interactions with other organelles (Banani et al., 2016; Alberti and Hyman, 2021; Wu et al., 2018; Lee et al., 2020; Liao et al., 2019; Friedman and Voeltz, 2011). Thus, our automated FLIM-FRET approach provides the potential to resolve functional subdomains within or between organelles to simultaneously evaluate organelle form and function in live cells.

Materials and methods

Molecular and cell biology reagents

DNA plasmids

Using Gibson Assembly, we generated LR clonase competent entry vectors (pENTR D-TOPO backbone) with N- or C-termini fluorescence tags (mTQ2, mNG, mScarlet, or HaloTag) with identical multiple cloning sites to pAcGFP1-C1 or -N1 (Clontech/Takara), and second-generation lentiviral destination expression plasmids (pHAGE backbone) driven by a mouse phosphoglycerate kinase promoter lacking mammalian selection genes. G3BP1, Dcp2, Dcp1A, and EDC3 were subcloned by restriction enzyme digest from previously published non-viral mammalian expression plasmids (Lee et al., 2020) and inserted into entry vectors with encoded fluorescent tags. The luminal ER marker, mCh-KDEL, consists of the BiP signal sequence, mCherry, and the KDEL retention sequence (ssBiP-mCh-KDEL), which was PCR amplified from an existing plasmid (Lee et al., 2020) and inserted into a pENTR D-TOPO backbone. DDX6 and Lsm14a were PCR amplified from a HEK293T cDNA library and inserted into entry vectors after XhoI and KpnI, or EcoRI and BamHI digestion, respectively. Genetically encoded fluorescent tags and genes within entry vectors were transferred into lentiviral destination plasmids by Gateway cloning.

DCP1A/1B DKO U-2 OS cells were generated by transient co-transfection of two expression plasmids encoding for Cas9 and *DCP1A* or *DCP1B* guide sequences with Lipofectamine 3000 followed by clonal selection. Gene and protein deletion were confirmed by PCR and western blot, respectively. Briefly, primers encoded with two guide sequences targeting a critical exon within *DCP1A* were used to PCR amplify an insert sequence encoding for constant region 3 (CR3) and the murine U6 promoter. The BsmBI-guide 1-CR3-mU6-guide 2-BsmBI amplicon was inserted into LentiCRISPRv2 plasmid (#52961; Addgene) by Golden Gate Assembly. The same cloning strategy was used to generate a LentiCRISPRv2 plasmid encoding two guide sequences targeting *DCP1B*.

DCP1A guides: 5′-CCACAATTTGTGGAATGAGA-3′ and 5′-GGACCTTATTCGTATATCGA-3′.
DCP1B guides: 5′-AGGTCTGCTTCTCCAAAGCA-3′ and 5′-GTGAGTCTTTCTTACTACAG-3′.
DDX6 Forward Primer Oligo: 5′-AGCACGGCCAGAACAGAGAAC-3′.
DDX6 Reverse Primer Oligo: 5′-TTAAGGTTTCTCATCTTCTACAGGCTCGC-3′.
Lsm14a Forward Primer Oligo: 5′-AGCGGGGGCACCCCTTACATC-3′.
Lsm14a Reverse Primer Oligo: 5′-TTAGGGTCCAAAAGCTGTGGTTTTCCTATATTCAAAATCC-3′.

Lentiviral packaging

Human embryonic kidney (HEK293T - CRL-3216) cells were obtained from the American Tissue Culture Collection (ATCC)

and maintained in Dulbecco's Modified Eagle Media (DMEM; Sigma-Aldrich) and 10% fetal bovine serum (FBS; VWR) without antibiotics. Approximately 80% confluent cells in 6-cm dishes were transfected by combining destination plasmid, and the second-generation packaging and envelope plasmids, psPAX2 (12260; Addgene) and pMD2.G (12259; Addgene) with Lipofectamine 3000. After 5–6 h of incubation, cells were rinsed and replenished with 5 ml of fresh media. Lentivirus-containing media was collected after 48 and 72 h, filtered with 0.45-µm polyether sulfone filters, and spun to remove debris. The two harvests were then pooled and spun at 21,000 rcf for 2 h in a microcentrifuge to concentrate lentivirus. After centrifugation, the supernatant was carefully removed and discarded. Lentivirus was resuspended with 500 µl of Lentivirus Stabilizer (OriGene), aliquoted, and stored at −80°C.

Stable cell line generation and cell line maintenance

Human osteosarcoma (U-2 OS - HTB-96) and alveolar basal epithelial (A549 - CCL-185) cells were obtained from ATCC and maintained in McCoy's or DMEM-F12 media (both-Sigma-Aldrich) supplemented with 10% FBS and penicillin/streptomycin (Life Technologies). Cell lines were tested for contamination at the start of experiments and every 3 wk after using a PCR-based mycoplasma test (Invivogen). All single- and multigene exogenous expression cell lines used in this manuscript were generated by combining 5 µg/ml polybrene (Sigma-Aldrich) with one or multiple lentiviruses, and transducing ∼80% confluent cells overnight followed by replenishing with fresh media for one recovery day. Cells were split twice over the course of three days prior to experiments on polyclonal cultures, seeded in 96-well plates for clonal selection, or isolated by fluorescence-activated cell sorting (FACS). FACS or clonal selection enabled the enrichment of cell populations with similar fluorescence expression levels, which exhibited quality-controlled organelle standards set by our immunofluorescence characterizations in U-2 OS and A549 cells of endogenous P-body and stress granule abundance and responses to oxidative stress, as well as ER morphology. All cells were maintained at 37°C, 5% CO_2, and 90% humidity.

Time-lapse microscopy

Microscope and incubator

Live-cell confocal FLIM was performed on a Stellaris 8 FALCON (Leica) confocal microscope equipped with a 78 MHz pulsed white light laser (440–790 nm), hybrid detectors with gallium arsenide phosphide photocathode front plate coupled with an avalanche diode, 1.40-NA plan-apochromat 63× oil immersion objective, and stage-top incubation and objective heater system (Okolab).

Capture settings and live imaging workflow

mTQ2 was captured with 440-nm excitation and a 460–490-nm emission detection window. mNG was captured with 504-nm excitation and a 520–550-nm emission detection window. mScarlet and JF549 were captured with 570-nm excitation and 585–700-nm emission detection windows. JF549 was captured with a suboptimal excitation wavelength to minimize cross-excitation of mNG. mCh was captured with 587-nm excitation and a 600–700-nm emission detection window. Non-overlapping tile scans with 512 × 512-pixel times were captured with a 150 Hz scan rate, 4× line accumulation, 3.0 zoom, and 0.12-µm pixel size. The incubation chamber was maintained at 37°C, 5% CO_2, and 90% humidity. Cells were imaged in their complete growth medium listed above. $NaAsO_2$ was dissolved in deionized water (dH_2O) to yield a 0.5 M stock solution just before treatment. $NaAsO_2$ was spiked into the microscope dish during time-lapse imaging to a final concentration of 0.5 mM. To track cells before and after stress, care was taken to avoid disturbing the dish during $NaAsO_2$ addition. LAS X Microscope Software (Leica) was used to operate the microscope and capture data.

Fluorescence image processing and analyses

Fluorescence intensity–based organelle segmentation

CellProfiler was used for intensity-based segmentation of ER, stress granules, and P-bodies. The ER was segmented using a modified CellProfiler workflow developed for ER morphology analysis (Garcia-Pardo et al., 2021). Stress granules and P-bodies were segmented with a custom CellProfiler workflow. Briefly, a Gaussian filter was first applied to intensity to increase signal-to-noise ratios (SNRs) between dilute and condensed phases. Primary objects were identified from filtered images using Otsu's thresholding algorithm. Particle number and area were computed and exported along with binary images.

Processing TCSPC data to generate unfiltered and filtered phasor plots

TCSPC data for experiments and FITC calibration were exported as raw .bin files from LASX FALCON (Leica) and converted to TIFF files in ImageJ. TIFF files for experiments and calibration were imported in the Fluorescence Lifetime Ultimate Explorer (FLUTE) Python GUI (graphical user interface), which then provided either unfiltered or median-filtered G and S coordinates. Unfiltered and median-filtered phasor plots were generated using our custom phasor plot Python script by weighting G and S coordinates with the intensity images. For wavelet-filtered phasor plots, unfiltered G and S coordinates from FLUTE were processed using our custom complex wavelet filter Python script. First, an Anscombe transform is applied to the Fourier coefficients and Intensity to shift G and S coordinate maps with approximate standard Gaussian distributions. A Dual-Tree Complex Wavelet Transform was then applied with nine filtering levels followed by an inverse Anscombe transform to generate wavelet-filtered coefficients and intensity, which were used to calculate wavelet-filtered G and S coordinates.

GMM algorithm for FLIM phasor-guided isolation of RNP condensate pixels

This section details the methodology behind our automated wavelet-filtered phasor plot segmentation approach to precisely isolate condensate pixels. Our GMM algorithm requires raw photon counts (fluorescence intensity data), wavelet-filtered G and S coordinates, and an accurate prediction of cluster number. However, lifetime clusters from undesired signal sources, such

as autofluorescence, might mislead the GMM resulting in the generation of inaccurate cluster positions. Therefore, we focused the GMM on a circular region of the phasor plot with a large defined radius centered around the ideal fluorophore lifetime by removing pixels outside of this circular region. The curated phasor plot enables the GMM to reproducibly identify two Gaussian, condition-blind center coordinates corresponding to the condensed and dilute phases of RNP condensate proteins, and one Gaussian center for membrane-bound organelles, such as the ER. Next, the ROI size for phasor plot segmentation of condensate pixels is determined by the covariance matrix generated by the GMM to locate cluster centers. Our GMM algorithm returns cluster centers, the magnitude and direction of the minimum covariance around the cluster center, and the maximum covariance magnitude and direction around the cluster center. For circular ROIs used to segment unfiltered FLIM phasor data, we use the minimum covariance value for the radius. For elliptical ROIs used to segment wavelet filtered FLIM phasor data, we use the minimum covariance value for the length of the short axis, maximum covariance value for the length of the long axis, and angle of rotation parallel to the direction of the maximum covariance value. Lastly, for elliptical ROIs used to segment dilute and condensed phases, we adjust the ROI size proportional to the partitioning of the condensate protein captured by using a covariance factor. For mNG-G3BP1, which has a low partition coefficient, we used 2.5 times the covariance to determine ROI size, whereas for mNG-DDX6, which has a higher partition coefficient, 3.0 times the covariance was used, respectively. This approach successfully segmented pixels residing in most, if not all, RNP condensates using the first harmonic wavelet-filtered phasor plots. Condensate-specific wavelet G and S coordinates are then used to build fluorescence lifetime histograms or generate condensate masks by performing an inverse Fourier transform.

Automated FLIM-FRET segmentation within RNP condensates

Reference donor measurements can be obtained from cells expressing only the mNG-Donor or from cells co-expressing mNG-Donor and Halo-Acceptor without JF549. Experimental donor measurements can be obtained from cells co-expressing the mNG-Donor and mScarlet-Acceptor or from the cells co-expressing mNG-Donor and Halo-Acceptor labeled with JF549. Donor FLIM TCSPC data from reference and experimental cells were transformed into unfiltered phasor plots to generate reference and experimental fluorescence lifetime images. To generate reference and experimental condensate masks, donor FLIM TCSPC data from reference and experimental cells were transformed into wavelet-filtered phasor plots, then segmented by the GMM using a covariance factor of 2.0 to evaluate FLIM-FRET in stress granules and P-bodies.

To obtain the mean donor lifetime of reference condensates (T_D), a condensate ROI list was generated from the reference mask in ImageJ using the Analyze particles function with a lower area limit set to 100 nm^2. The ROI list was overlayed on the reference fluorescence lifetime image to obtain mean fluorescence lifetime measurements for individual condensates, which was used to calculate T_D.

To obtain mean FRET efficiencies (E_{FRET}) for individual condensates, a condensate ROI list was generated from the experimental mask in ImageJ using the Analyze particles function with a lower area limit set to 100 nm^2. The ROI list was overlayed on the reference fluorescence lifetime image to obtain mean fluorescence lifetime measurements for individual condensates. FRET efficiency was calculated for individual condensates or the total condensate population with the following equation (Clegg, 1995):

$$E_{FRET} = 1 - \frac{(T1_{D+A} + T2_{D+A} + T3_{D+A} + T[n]_{D+A})}{(T_D \bullet n)}$$

where T_D = mean donor lifetime of condensates from reference cells emitting only donor fluorescence, T_{D+A} = mean donor lifetime of condensates from experimental cells, and n = total number of condensates.

Immunofluorescence

U-2 OS cells were plated on 35-mm dishes with glass bottoms. Cells were fixed using a 37°C solution of 4% paraformaldehyde and 4% sucrose in phosphate-buffered saline (PBS) for 10 min. Cells were permeabilized with 0.1% triton in PBS for 4 min and blocked with 5% normal donkey serum in PBS for 1 h at room temperature. Cells were incubated with primary mouse monoclonal DDX6 antibody (1:100, SAB4200837; MilliporeSigma) in blocking solution for 1 h at room temperature, washed with PBS three times, and then incubated with donkey anti-mouse secondary antibody conjugated to AlexaFluor-647 (1:400, A-31571; Invitrogen) in blocking solution for 1 h at room temperature. Hoechst (Thermo Fisher Scientific) was used for nuclear staining.

Western blot analysis

Cells were dissociated using Trypsin-EDTA (Thermo Fisher Scientific) and collected by centrifugation at 200 rcf for 2 min. Cell pellets were resuspended with Laemmli's sample buffer (BioRad) supplemented with fresh β-mercaptoethanol (BioRad) and heated for 5 min at 95°C. Proteins from whole-cell lysates were resolved by size using SDS-PAGE in precast 4–20% Mini-PROTEAN TGX Stain-Free Gradient Gels (BioRad) and transferred to polyvinylidene difluoride membranes (Thermo Fisher Scientific). The following antibodies were used for western blot: DCP1A (1:200, SC-100706; Santa Cruz), DCP1B (1:500, 13233S; Cell Signaling Technologies), and COX IV (1:1,000, 48448; Cell Signaling Technologies). Immunolabeled membranes were then incubated in ECL Prime Western Blotting Detection Reagent (Cytiva) and imaged using an Azure Imaging System (Azure Biosystems).

Statistics

P values for experiments involving the comparison of FRET efficiencies of individual P-bodies across two conditions (basal versus stressed) were determined using parametric, nested *T* tests where a normal distribution is assumed, but not formally tested. For experiments involving three conditions (basal, stressed, and recovery), statistical significance was determined using one-way ANOVA, where a normal distribution was assumed. Comparison of intensity versus phasor-based segmentation

and of Mander's colocalization coefficients before and after stress was done using paired Student's *T* tests.

Online supplemental material

Fig. S1 shows that mNG emits photons with mono-exponential decay. Fig. S2 shows that phasor plot filtering is a universal approach to segment stress granule FLIM data, which is independent of the type of FLIM system. Fig. S3 Shows that FLIM phasor plot-guided segmentation outperforms traditional intensity-threshold segmentation approaches for generating ER masks. Fig. S4 shows unfiltered and filtered phasor plots of mNG localized to condensed and dilute phases. Fig. S5 shows stress granule FLIM-FRET detects G3BP1 dimerization in live cells. Fig. S6 shows context-dependent interactions between subunits of the mRNA decapping complex occur within P-bodies. Fig. S7 shows that gene ablation of *Dcp1A* and *Dcp1B* in U-2 OS cells resulted in an increase in P-body size and abundance.

Data availability

All data is available in the main text. Raw and processed data available upon request. Complex wavelet filtering and GMM segmentation scripts are available on GitHub (https://github.com/LeeLabBCM/ComplexWaveletFilter) and ImageJ Macros scripts will be made upon request.

Acknowledgments

We thank C. Stringari, S.M. Fessehaye, H. Wu, E. Sawyer, S. Gumbin, and S. Hartig for helpful insights and scientific discussions.

J.E. Lee obtained funding for the work, which was supported by the Cancer Prevention and Research Institute of Texas (CPRIT RR200065) and the National Institutes of Health (R35GM151054). J.E. Lee is a CPRIT Scholar in Cancer Research. J.M. Marcus, L.E. Fahim, N.D. Powell, Z.A. Ralston, K. Walgamotte were supported by a grant from CPRIT (RR200065). J.M. Marcus, L.E. Fahim, N.D. Powell were also supported by grants from the NIH, T32ES027801 and R35GM151054.

Author contributions: L.E. Fahim: Data curation, Formal analysis, Investigation, Methodology, Software, Validation, Visualization, Writing - review and editing, J.M. Marcus: Data curation, Formal analysis, Investigation, Methodology, Software, Validation, Visualization, Writing - review and editing, N.D. Powell: Formal analysis, Investigation, Software, Validation, Visualization, Writing - review and editing, Z.A. Ralston: Resources, Writing - review and editing, K. Walgamotte: Data curation, Formal analysis, Investigation, Writing - review and editing, E. Perego: Investigation, Validation, Writing - review and editing, G. Vicidomini: Conceptualization, Writing - review and editing, A. Rossetta: Conceptualization, Methodology, Software, Validation, Writing - review and editing, J.E. Lee: Conceptualization, Data curation, Funding acquisition, Investigation, Methodology, Project administration, Resources, Supervision, Validation, Visualization, Writing - original draft, Writing - review and editing.

Disclosures: G. Vicidomini reported holding shares of Genoa Instruments. A. Rossetta reported being the CEO and founder of FLIM LABS S.r.l., an LLC based in Italy that specializes in developing hardware and software solutions for fluorescence lifetime lmaging (FLIM) and spectroscopy. The company focuses on advancing and commercializing technologies in the fluorescence lifetime analysis field, which are closely related to the subject matter of this paper. A. Rossetta acknowledges this relationship and affirms his commitment to maintaining the scientific integrity of this work, ensuring that all interpretations and conclusions are objective and independent of any potential commercial motivations. No other disclosures were reported.

Submitted: 17 November 2023
Revised: 12 August 2024
Accepted: 23 September 2024

References

Abramson, J., J. Adler, J. Dunger, R. Evans, T. Green, A. Pritzel, O. Ronneberger, L. Willmore, A.J. Ballard, J. Bambrick, et al. 2024. Accurate structure prediction of biomolecular interactions with AlphaFold 3. *Nature*. 630:493–500. https://doi.org/10.1038/s41586-024-07487-w

Alberti, S., and A.A. Hyman. 2021. Biomolecular condensates at the nexus of cellular stress, protein aggregation disease and ageing. *Nat. Rev. Mol. Cell Biol.* 22:196–213. https://doi.org/10.1038/s41580-020-00326-6

Antonicka, H., F. Sasarman, T. Nishimura, V. Paupe, and E.A. Shoubridge. 2013. The mitochondrial RNA-binding protein GRSF1 localizes to RNA granules and is required for posttranscriptional mitochondrial gene expression. *Cell Metab.* 17:386–398. https://doi.org/10.1016/j.cmet.2013.02.006

Banani, S.F., A.M. Rice, W.B. Peeples, Y. Lin, S. Jain, R. Parker, and M.K. Rosen. 2016. Compositional control of phase-separated cellular bodies. *Cell*. 166:651–663. https://doi.org/10.1016/j.cell.2016.06.010

Barkley, R.J.R., J.C. Crowley, A.J. Brodrick, W.R. Zipfel, and J.S.L. Parker. 2024. Fluorescent protein tags affect the condensation properties of a phase-separating viral protein. *Mol. Biol. Cell*. 35:ar100. https://doi.org/10.1091/mbc.E24-01-0013

Blake, L.A., L. Watkins, Y. Liu, T. Inoue, and B. Wu. 2024. A rapid inducible RNA decay system reveals fast mRNA decay in P-bodies. *Nat. Commun.* 15:2720. https://doi.org/10.1038/s41467-024-46943-z

Brandmann, T., H. Fakim, Z. Padamsi, J.-Y. Youn, A.-C. Gingras, M.R. Fabian, and M. Jinek. 2018. Molecular architecture of LSM14 interactions involved in the assembly of mRNA silencing complexes. *EMBO J.* 37: e97869. https://doi.org/10.15252/embj.201797869

Bray, M.-A., and A.E. Carpenter. 2018. Quality control for high-throughput imaging experiments using machine learning in cellprofiler. *Methods Mol. Biol.* 1683:89–112. https://doi.org/10.1007/978-1-4939-7357-6_7

Brothers, W.R., F. Ali, S. Kajjo, and M.R. Fabian. 2023. The EDC4-XRN1 interaction controls P-body dynamics to link mRNA decapping with decay. *EMBO J.* 42:e113933. https://doi.org/10.15252/embj.2023113933

Chang, C.-T., N. Bercovich, B. Loh, S. Jonas, and E. Izaurralde. 2014. The activation of the decapping enzyme DCP2 by DCP1 occurs on the EDC4 scaffold and involves a conserved loop in DCP1. *Nucleic Acids Res.* 42: 5217–5233. https://doi.org/10.1093/nar/gku129

Charenton, C., V. Taverniti, C. Gaudon-Plesse, R. Back, B. Séraphin, and M. Graille. 2016. Structure of the active form of Dcp1-Dcp2 decapping enzyme bound to m^7GDP and its Edc3 activator. *Nat. Struct. Mol. Biol.* 23: 982–986. https://doi.org/10.1038/nsmb.3300

Chen, Y., J.D. Mills, and A. Periasamy. 2003. Protein localization in living cells and tissues using FRET and FLIM. *Differentiation*. 71:528–541. https://doi.org/10.1111/j.1432-0436.2003.07109007.x

Cho, D.-S.C., W. Yang, J.T. Lee, R. Shiekhattar, J.M. Murray, and K. Nishikura. 2003. Requirement of dimerization for RNA editing activity of adenosine deaminases acting on RNA. *J. Biol. Chem.* 278:17093–17102. https://doi.org/10.1074/jbc.M213127200

Clegg, R.M. 1995. Fluorescence resonance energy transfer. *Curr. Opin. Biotechnol.* 6:103–110. https://doi.org/10.1016/0958-1669(95)80016-6

Csordás, G., P. Várnai, T. Golenár, S. Roy, G. Purkins, T.G. Schneider, T. Balla, and G. Hajnóczky. 2010. Imaging interorganelle contacts and local calcium dynamics at the ER-mitochondrial interface. *Mol. Cell*. 39: 121–132. https://doi.org/10.1016/j.molcel.2010.06.029

Currie, S.L., W. Xing, D. Muhlrad, C.J. Decker, R. Parker, and M.K. Rosen. 2023. Quantitative reconstitution of yeast RNA processing bodies. *Proc. Natl. Acad. Sci. USA*. 120:e2214064120. https://doi.org/10.1073/pnas.2214064120

Decker, C.J., and R. Parker. 2012. P-bodies and stress granules: Possible roles in the control of translation and mRNA degradation. *Cold Spring Harb. Perspect. Biol.* 4:a012286. https://doi.org/10.1101/cshperspect.a012286

Digman, M.A., V.R. Caiolfa, M. Zamai, and E. Gratton. 2008. The phasor approach to fluorescence lifetime imaging analysis. *Biophys. J.* 94: L14–L16. https://doi.org/10.1529/biophysj.107.120154

Eulalio, A., I. Behm-Ansmant, D. Schweizer, and E. Izaurralde. 2007. P-body formation is a consequence, not the cause, of RNA-mediated gene silencing. *Mol. Cell. Biol.* 27:3970–3981. https://doi.org/10.1128/MCB.00128-07

Fenger-Grøn, M., C. Fillman, B. Norrild, and J. Lykke-Andersen. 2005. Multiple processing body factors and the ARE binding protein TTP activate mRNA decapping. *Mol. Cell.* 20:905–915. https://doi.org/10.1016/j.molcel.2005.10.031

Freibaum, B.D., J. Messing, P. Yang, H.J. Kim, and J.P. Taylor. 2021. High-fidelity reconstitution of stress granules and nucleoli in mammalian cellular lysate. *J. Cell Biol.* 220:e202009079. https://doi.org/10.1083/jcb.202009079

Friedman, J.R., and G.K. Voeltz. 2011. The ER in 3D: A multifunctional dynamic membrane network. *Trends Cell Biol.* 21:709–717. https://doi.org/10.1016/j.tcb.2011.07.004

Garcia-Pardo, M.E., J.C. Simpson, and N.C. O'Sullivan. 2021. A novel automated image analysis pipeline for quantifying morphological changes to the endoplasmic reticulum in cultured human cells. *BMC Bioinformatics*. 22:427. https://doi.org/10.1186/s12859-021-04334-x

Gottlieb, D., B. Asadipour, P. Kostina, T.P.L. Ung, and C. Stringari. 2023. FLUTE: A Python GUI for interactive phasor analysis of FLIM data. *Biol. Imaging*. 3:e21. https://doi.org/10.1017/S2633903X23000211

Heim, R., and R.Y. Tsien. 1996. Engineering green fluorescent protein for improved brightness, longer wavelengths and fluorescence resonance energy transfer. *Curr. Biol.* 6:178–182. https://doi.org/10.1016/s0960-9822(02)00450-5

Hinde, E., M.A. Digman, C. Welch, K.M. Hahn, and E. Gratton. 2012. Biosensor Förster resonance energy transfer detection by the phasor approach to fluorescence lifetime imaging microscopy. *Microsc. Res. Tech.* 75:271–281. https://doi.org/10.1002/jemt.21054

Hubstenberger, A., M. Courel, M. Bénard, S. Souquere, M. Ernoult-Lange, R. Chouaib, Z. Yi, J.-B. Morlot, A. Munier, M. Fradet, et al. 2017. P-body purification reveals the condensation of repressed mRNA regulons. *Mol. Cell*. 68:144–157.e5. https://doi.org/10.1016/j.molcel.2017.09.003

Ibrahim, F., J. Oppelt, M. Maragkakis, and Z. Mourelatos. 2021. TERA-seq: True end-to-end sequencing of native RNA molecules for transcriptome characterization. *Nucleic Acids Res.* 49:e115. https://doi.org/10.1093/nar/gkab713

Jonas, S., and E. Izaurralde. 2013. The role of disordered protein regions in the assembly of decapping complexes and RNP granules. *Genes Dev.* 27: 2628–2641. https://doi.org/10.1101/gad.227843.113

Jourdain, A.A., M. Koppen, M. Wydro, C.D. Rodley, R.N. Lightowlers, Z.M. Chrzanowska-Lightowlers, and J.-C. Martinou. 2013. GRSF1 regulates RNA processing in mitochondrial RNA granules. *Cell Metab.* 17:399–410. https://doi.org/10.1016/j.cmet.2013.02.005

Kedersha, N.L., M. Gupta, W. Li, I. Miller, and P. Anderson. 1999. RNA-binding proteins TIA-1 and TIAR link the phosphorylation of eIF-2 alpha to the assembly of mammalian stress granules. *J. Cell Biol.* 147: 1431–1442. https://doi.org/10.1083/jcb.147.7.1431

Krishna, R., J. Wang, W. Ahern, P. Sturmfels, P. Venkatesh, I. Kalvet, G.R. Lee, F.S. Morey-Burrows, I. Anishchenko, I.R. Humphreys, et al. 2024. Generalized biomolecular modeling and design with RoseTTAFold All-Atom. *Science*. 384:eadl2528. https://doi.org/10.1126/science.adl2528

Lambert, T.J. 2019. FPbase: A community-editable fluorescent protein database. *Nat. Methods*. 16:277–278. https://doi.org/10.1038/s41592-019-0352-8

Lee, J.E., P.I. Cathey, H. Wu, R. Parker, and G.K. Voeltz. 2020. Endoplasmic reticulum contact sites regulate the dynamics of membraneless organelles. *Science*. 367:eaay7108. https://doi.org/10.1126/science.aay7108

Liao, Y.-C., M.S. Fernandopulle, G. Wang, H. Choi, L. Hao, C.M. Drerup, R. Patel, S. Qamar, J. Nixon-Abell, Y. Shen, et al. 2019. RNA granules Hitchhike on lysosomes for long-distance transport, using Annexin A11 as a molecular tether. *Cell*. 179:147–164.e20. https://doi.org/10.1016/j.cell.2019.08.050

Lin, H.-J., P. Herman, and J.R. Lakowicz. 2003. Fluorescence lifetime-resolved pH imaging of living cells. *Cytometry A*. 52:77–89. https://doi.org/10.1002/cyto.a.10028

Malacrida, L., and E. Gratton. 2018. LAURDAN fluorescence and phasor plots reveal the effects of a H_2O_2 bolus in NIH-3T3 fibroblast membranes dynamics and hydration. *Free Radic. Biol. Med.* 128:144–156. https://doi.org/10.1016/j.freeradbiomed.2018.06.004

Malacrida, L., S. Ranjit, D.M. Jameson, and E. Gratton. 2021. The phasor plot: A universal circle to advance fluorescence lifetime analysis and interpretation. *Annu. Rev. Biophys.* 50:575–593. https://doi.org/10.1146/annurev-biophys-062920-063631

Mangiarotti, A., M. Siri, N.W. Tam, Z. Zhao, L. Malacrida, and R. Dimova. 2023. Biomolecular condensates modulate membrane lipid packing and hydration. *Nat. Commun.* 14:6081. https://doi.org/10.1038/s41467-023-41709-5

Mariani, V., M. Biasini, A. Barbato, and T. Schwede. 2013. lDDT: A local superposition-free score for comparing protein structures and models using distance difference tests. *Bioinformatics*. 29:2722–2728. https://doi.org/10.1093/bioinformatics/btt473

Matheny, T., B.S. Rao, and R. Parker. 2019. Transcriptome-wide comparison of stress granules and P-bodies reveals that translation plays a major role in RNA partitioning. *Mol. Cell. Biol.* 39:e00313–e00319. https://doi.org/10.1128/MCB.00313-19

Moon, S.L., T. Morisaki, A. Khong, K. Lyon, R. Parker, and T.J. Stasevich. 2019. Multicolour single-molecule tracking of mRNA interactions with RNP granules. *Nat. Cell Biol.* 21:162–168. https://doi.org/10.1038/s41556-018-0263-4

Otsu, N. 1979. A threshold selection method from gray-level histograms. *IEEE*. 9:62–66. https://doi.org/10.1109/TSMC.1979.4310076

Perego, E., S. Zappone, F. Castagnetti, D. Mariani, E. Vitiello, J. Rupert, E. Zacco, G.G. Tartaglia, I. Bozzoni, E. Slenders, and G. Vicidomini. 2023. Single-photon microscopy to study biomolecular condensates. *Nat. Commun.* 14:8224. https://doi.org/10.1038/s41467-023-43969-7

Pliss, A., S.M. Levchenko, L. Liu, X. Peng, T.Y. Ohulchanskyy, I. Roy, A.N. Kuzmin, J. Qu, and P.N. Prasad. 2019. Cycles of protein condensation and discharge in nuclear organelles studied by fluorescence lifetime imaging. *Nat. Commun.* 10:455. https://doi.org/10.1038/s41467-019-08354-3

Riback, J.A., L. Zhu, M.C. Ferrolino, M. Tolbert, D.M. Mitrea, D.W. Sanders, M.-T. Wei, R.W. Kriwacki, and C.P. Brangwynne. 2020. Composition-dependent thermodynamics of intracellular phase separation. *Nature*. 581:209–214. https://doi.org/10.1038/s41586-020-2256-2

Rossetta, A., E. Slenders, M. Donato, S. Zappone, F. Fersini, M. Bruno, F. Diotalevi, L. Lanzanò, S. Koho, G. Tortarolo, et al. 2022. The BrightEyes-TTM as an open-source time-tagging module for democratising single-photon microscopy. *Nat. Commun.* 13:7406. https://doi.org/10.1038/s41467-022-35064-0

Sanders, D.W., N. Kedersha, D.S.W. Lee, A.R. Strom, V. Drake, J.A. Riback, D. Bracha, J.M. Eeftens, A. Iwanicki, A. Wang, et al. 2020. Competing protein-RNA interaction networks control multiphase intracellular organization. *Cell*. 181:306–324.e28. https://doi.org/10.1016/j.cell.2020.03.050

Schirle, N.T., J. Sheu-Gruttadauria, and I.J. MacRae. 2014. Structural basis for microRNA targeting. *Science*. 346:608–613. https://doi.org/10.1126/science.1258040

Shaner, N.C., G.G. Lambert, A. Chammas, Y. Ni, P.J. Cranfill, M.A. Baird, B.R. Sell, J.R. Allen, R.N. Day, M. Israelsson, et al. 2013. A bright monomeric green fluorescent protein derived from Branchiostoma lanceolatum. *Nat. Methods*. 10:407–409. https://doi.org/10.1038/nmeth.2413

Tibble, R.W., A. Depaix, J. Kowalska, J. Jemielity, and J.D. Gross. 2021. Biomolecular condensates amplify mRNA decapping by biasing enzyme conformation. *Nat. Chem. Biol.* 17:615–623. https://doi.org/10.1038/s41589-021-00774-x

Vallmitjana, A., B. Torrado, and E. Gratton. 2021. Phasor-based image segmentation: Machine learning clustering techniques. *Biomed. Opt. Express*. 12:3410–3422. https://doi.org/10.1364/BOE.422766

Wang, P., F. Hecht, G. Ossato, S. Tille, S.E. Fraser, and J.A. Junge. 2021. Complex wavelet filter improves FLIM phasors for photon starved imaging experiments. *Biomed. Opt. Express*. 12:3463–3473. https://doi.org/10.1364/BOE.420953

Weber, G. 1981. Resolution of the fluorescence lifetimes in a heterogeneous system by phase and modulation measurements. *J. Phys. Chem.* 85: 953–958. https://doi.org/10.1021/j150608a006

Wheeler, J.R., T. Matheny, S. Jain, R. Abrisch, and R. Parker. 2016. Distinct stages in stress granule assembly and disassembly. *Elife*. 5:e18413. https://doi.org/10.7554/eLife.18413

Wu, H., P. Carvalho, and G.K. Voeltz. 2018. Here, there, and everywhere: The importance of ER membrane contact sites. *Science*. 361:eaan5835. https://doi.org/10.1126/science.aan5835

Supplemental material

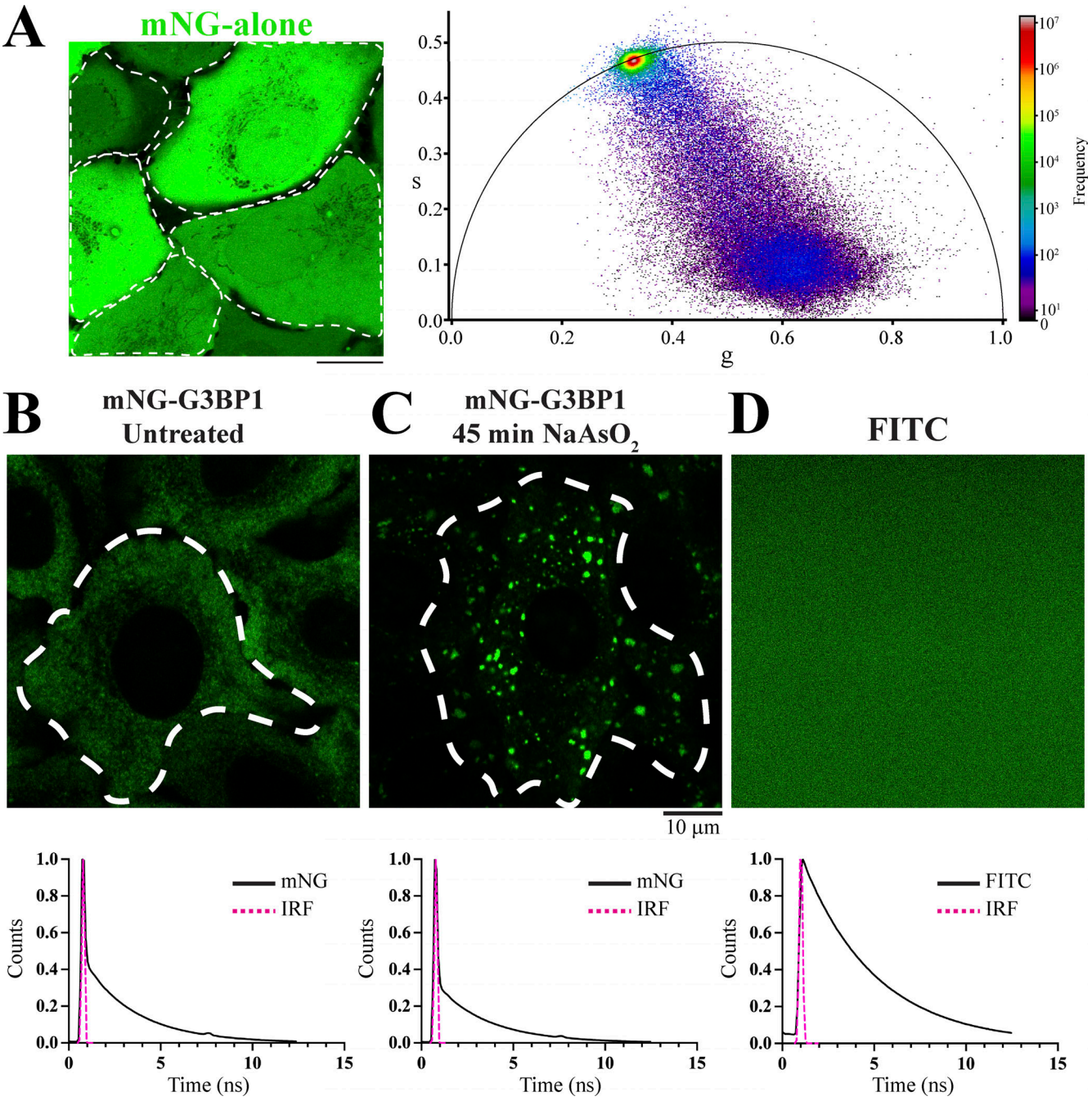

Figure S1. **mNG emits photons with mono-exponential decay. (A)** Fluorescence intensity image of U-2 OS cells stably expressing mNG and the corresponding wavelet-filtered phasor plot. **(B–D)** Fluorescence intensity images (top) and decay curves (bottom) of the same cells captured before (B) and after 45 min of oxidative stress (C), and a FITC image for calibration. The instrument response function (IRF) curve is highlighted in magenta. Scale bars = 10 µm.

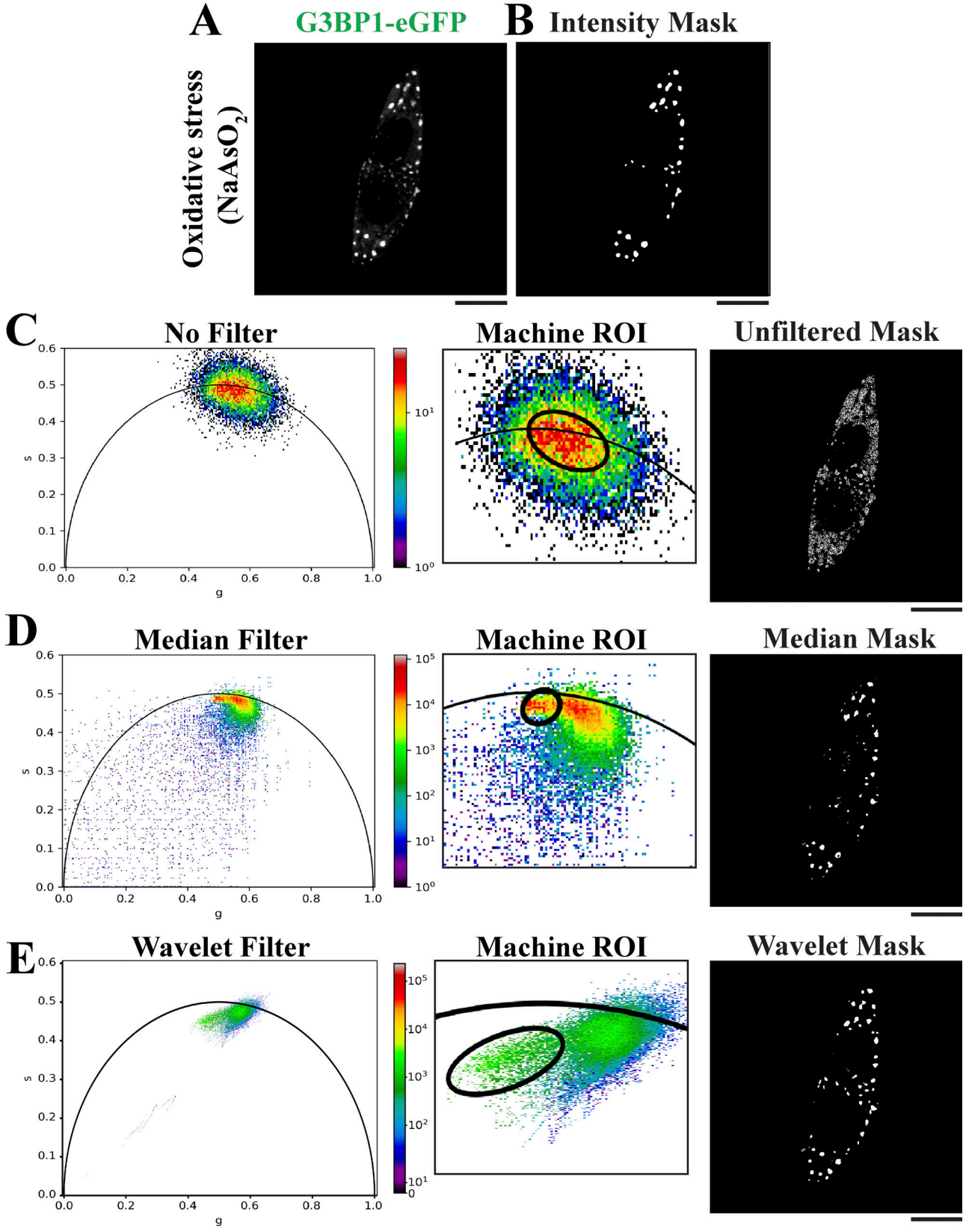

Figure S2. **Phasor plot filtering is a universal approach to segment stress granule FLIM data, which is independent of the type of FLIM system. (A)** Fluorescence intensity image of neuroblastoma (SK-N-BE) cells stably expressing G3BP1-eGFP captured using the BrightEyes time-tagging FLIM module (Perego et al., 2023; Rossetta et al., 2022). **(B)** Intensity-threshold mask generated with Cell Profiler. **(C–E)** Unfiltered, median-filtered, and complex wavelet-filtered G and S coordinates from a single FLIM image were plotted on phasor plots with a 1% threshold of the pixel with the highest photon counts, followed by segmentation using a GMM-covariance-derived ROI to produce masks. Scale bars = 10 µm.

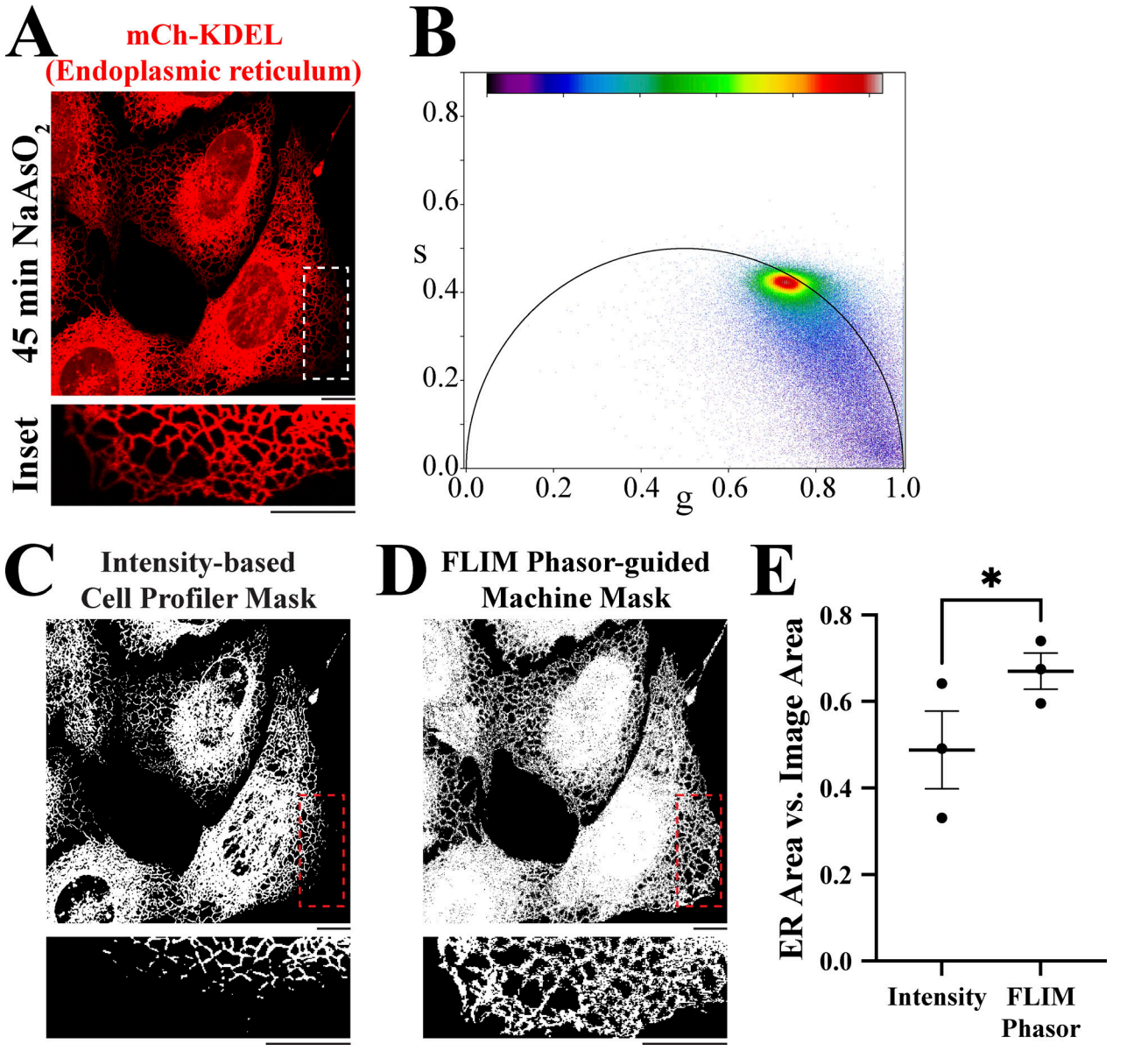

Figure S3. **FLIM phasor plot-guided segmentation outperforms traditional intensity-threshold segmentation approaches for generating ER masks. (A and B)** Fluorescence intensity image of U-2 OS cells stably expressing mCh-KDEL and the corresponding unthresholded, wavelet-filtered phasor plot. **(C)** Intensity-threshold mask generated with Cell Profiler. Inset demonstrates an incomplete mask coverage of ER tubules. **(D)** ER mask generated by phasor plot segmentation. Inset highlights the ability to segment dim ER tubules. **(E)** Intensity versus FLIM was compared by paired Student's *T* test with mean and SE displayed. *P = 0.0331. *N* = 3 biological replicates with *n* = 61 cells. Scale bars = 10 µm.

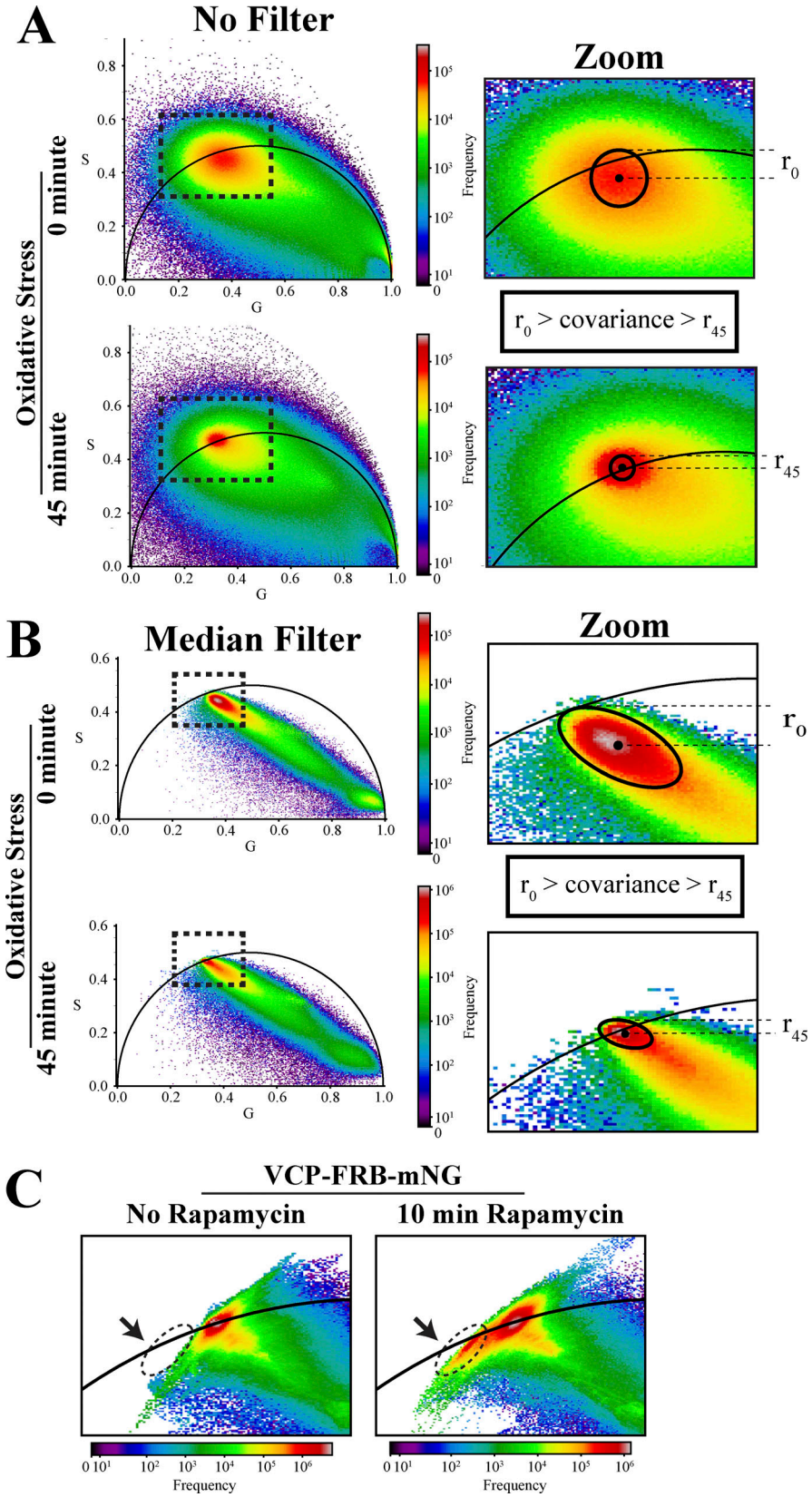

Figure S4. **Unfiltered and filtered phasor plots of mNG localized to condensed and dilute phases. (A and B)** Unfiltered and median-filtered, unthresholded phasor plots of mNG-G3BP1 captured from U-2 OS cells in Fig. 1, B–D before and after treatment with 0.5 mM $NaAsO_2$. Phasor plots include pixels accumulated from FLIM tile-scan images. The insets highlight GMM-generated ROIs, which were determined by the covariance of fluorescence lifetime clusters. **(C)** Unthresholded, wavelet-filtered phasor plots corresponding to Fig. 1, E–G of VCP-FRB-mNG before and after VCP recruitment to stress granules with rapamycin.

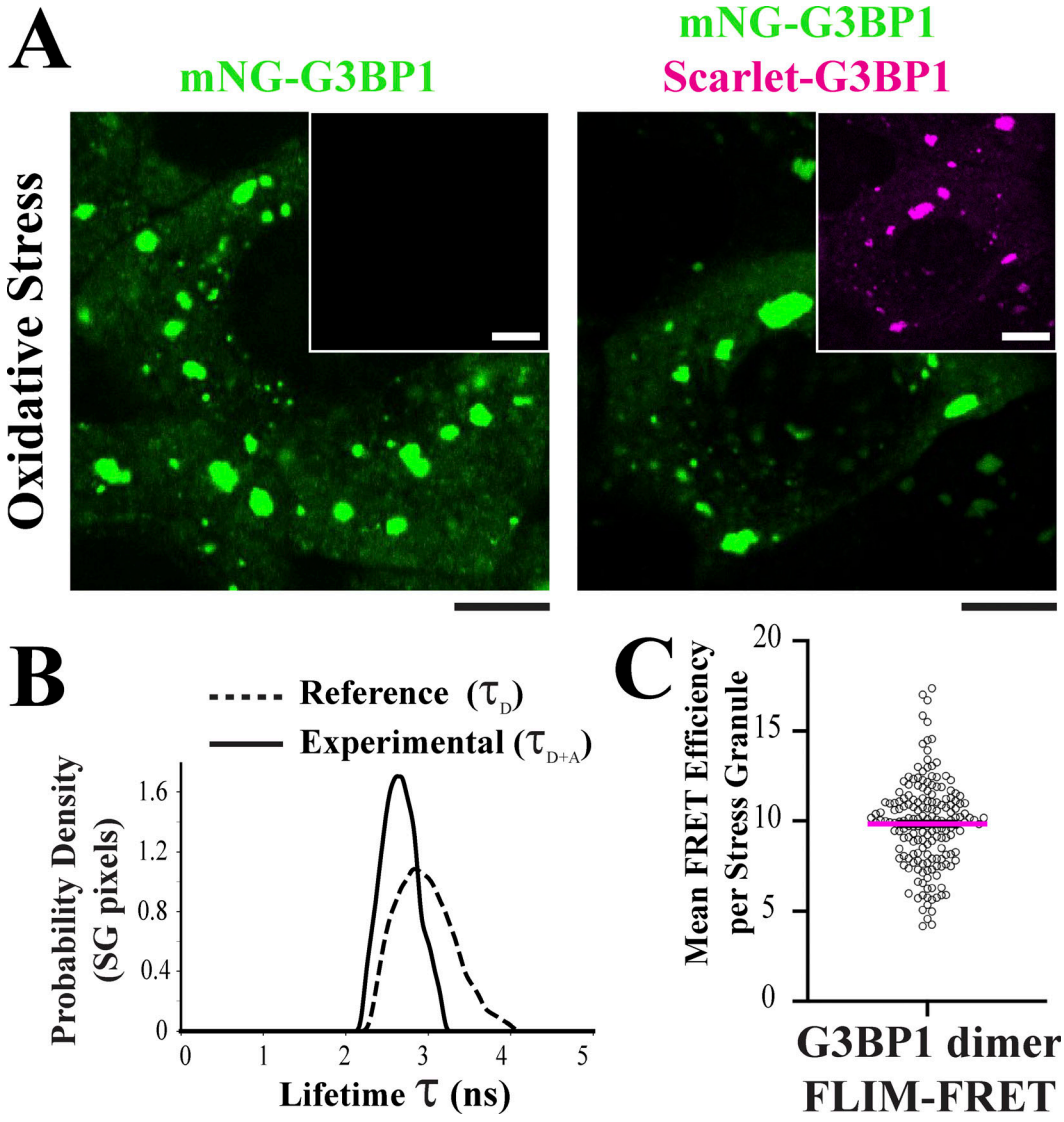

Figure S5. **Stress granule FLIM-FRET detects G3BP1 dimerization in live cells. (A)** Reference and experimental A549 cells expressing mNG-G3BP1 without and with mScarlet-G3BP1, respectively, were captured by FLIM after a 45-min treatment with $NaAsO_2$. **(B)** Fluorescence lifetime kernel density curves mNG-G3BP1 from reference and experimental cells. Scale bars = 5 µm. **(C)** Mean FRET efficiencies of individual stress granules are plotted with the mean highlighted (magenta). *n* = 30 reference cells and *n* = 27 experimental cells across three biological replicates.

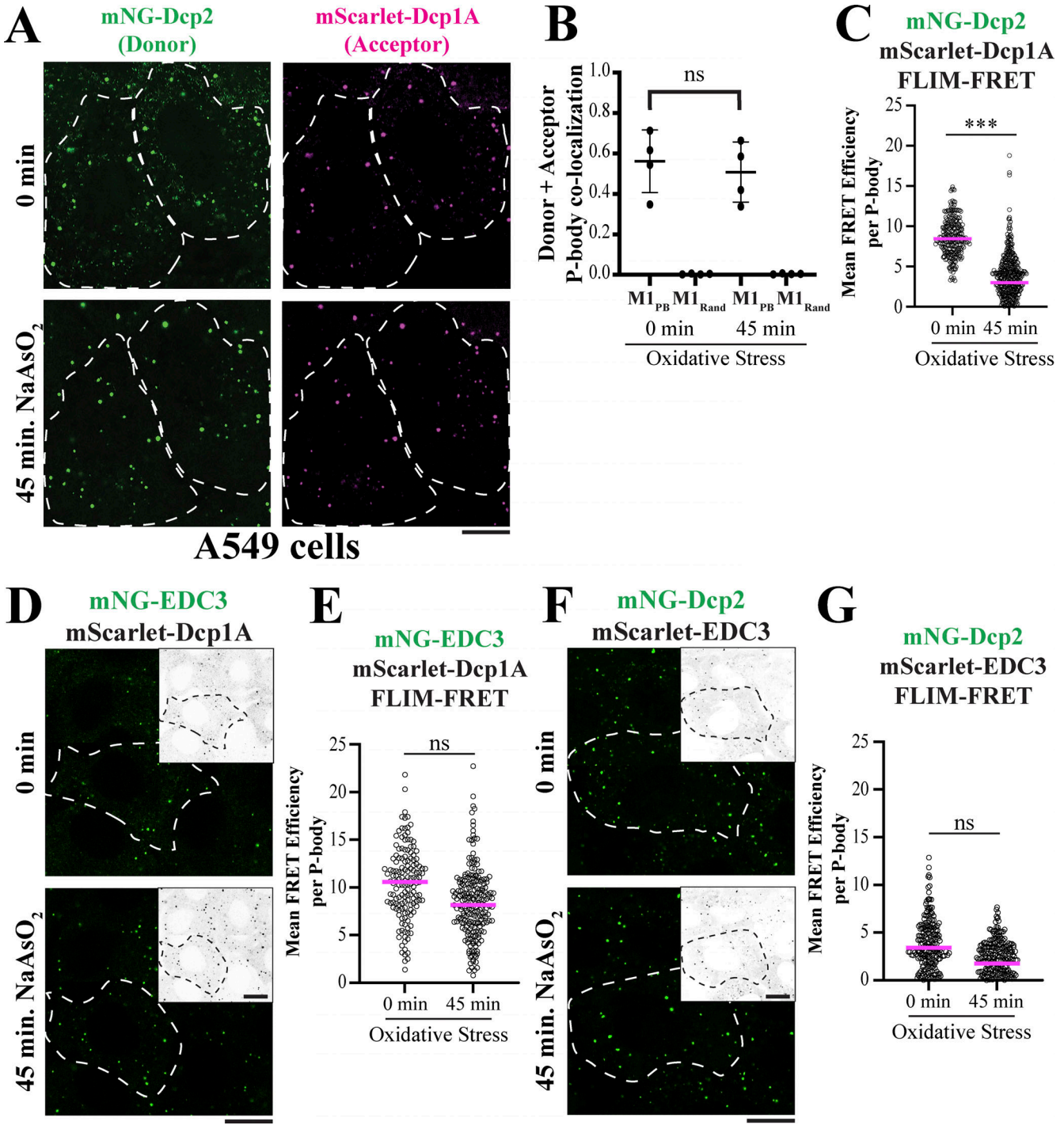

Figure S6. **Context-dependent interactions between subunits of the mRNA decapping complex occur within P-bodies. (A)** A549 cell lines stably co-expressing mNG-Dcp2 (green) and mScarlet-Dcp1A (magenta) were captured before and after treatment with 0.5 mM $NaAsO_2$. **(B)** FLIM-phasor-guided masks were generated from mNG-Dcp2 and mScarlet-Dcp1A images to yield Mander's colocalization coefficient before and after oxidative stress. Statistical significance was determined using a paired Student's *T* test with mean and SE displayed. As a control, image tiles were randomized by shuffling prior colocalization analyses to ensure that Dcp2 and Dcp1A were not colocalizing by chance. **(C)** Mean FRET efficiencies between Dcp2 and Dcp1A in individual P-bodies are plotted with the mean highlighted (magenta). **(A–C)** *N* = 4 biological replicates with *n* = 194 cells. **(D–G)** Fluorescence intensity images of A549 cells expressing (D) mNG-EDC3 and mScarlet-Dcp1A or (*n* = 179 cells) (F) mNG-Dcp2 and mScarlet-EDC3 (*n* = 186 cells) were evaluated for condensate FLIM-FRET in panels E and G, respectively. *N* = 3 biological replicates. **(C, E, and G)** Statistical significance was determined by Student's *T* test. ***P < 0.0001. All scale bars = 10 µm.

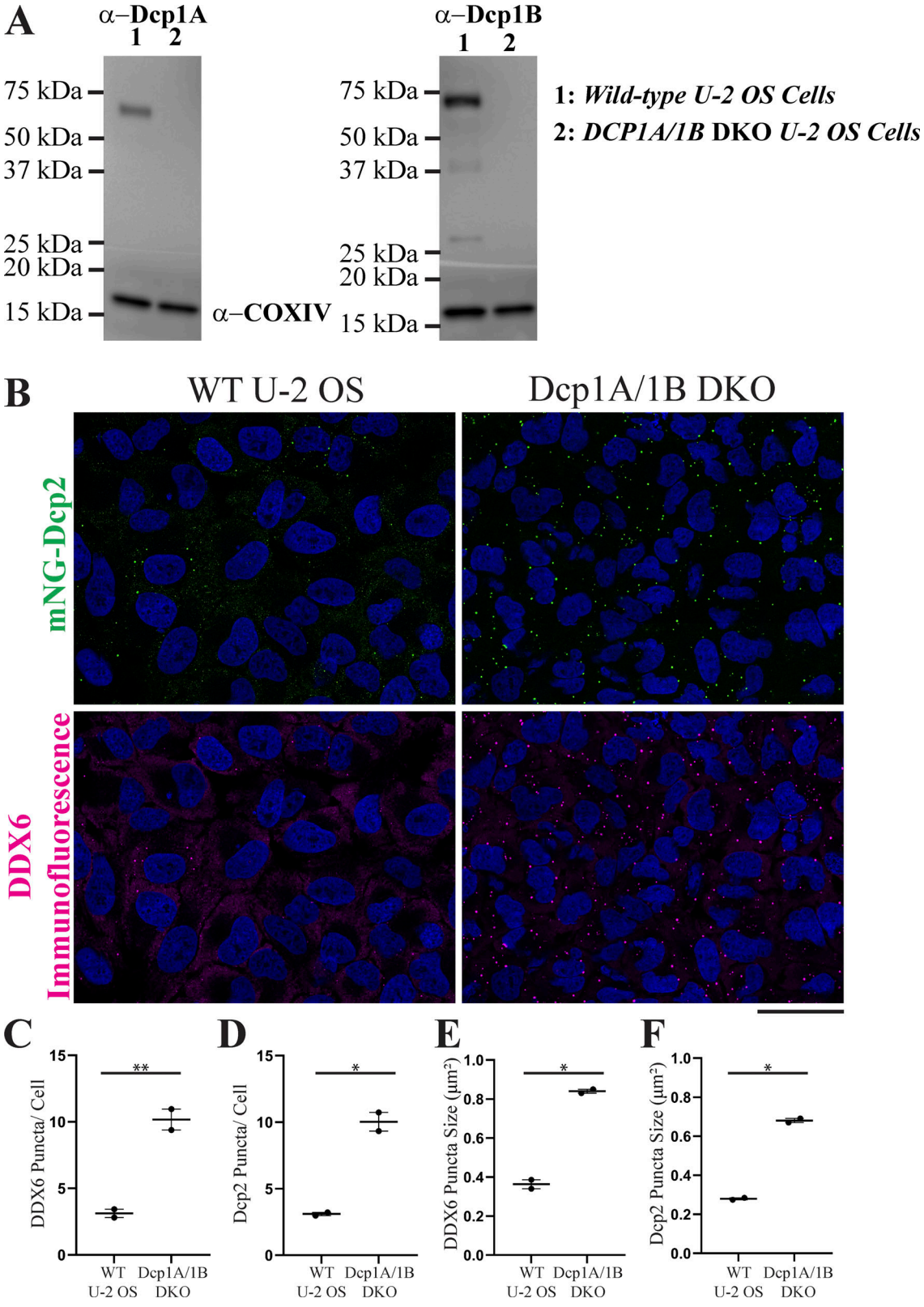

Figure S7. **Gene ablation of *Dcp1A* and *Dcp1B* in U-2 OS cells resulted in an increase in P-body size and abundance. (A)** *Dcp1A* and *Dcp1B* DKO U-2 OS cells were confirmed by western blot analyses of Dcp1A and Dcp1B antibodies. COXIV antibody was used as a loading control. **(B)** Immunofluorescence of DDX6 was performed in *wild-type* and *Dcp1A/1B* DKO cells stably expressing mNG-Dcp2. Nuclei were labeled with Hoecsht. Tile-scan images were captured with a 60× objective on a laser-scanning confocal microscope. **(C–F)** The nuclear stain was used to approximate cell number. Particle analyses of endogenous DDX6 and mNG-Dcp2 puncta were performed to obtain (C and D) P-body numbers per cell, and (E and F) area per P-body. *N* = 2 biological replicates. *P < 0.01, **P < 0.001. Source data are available for this figure: SourceData FS7.